Aalto University
School of Chemical
Engineering

Iiris Hakaste

FÖRSTER RESONANCE ENERGY TRANSFER ANALYSIS OF A DYNAMIC DNA ORIGAMI NANOCAPSULE

Master's Programme in Life Science Technologies
Major in Biosystems and Biomaterials Engineering

Master's thesis for the degree of Master of Science in Technology submitted for inspection, Espoo, February 16, 2019.

Supervisor: Professor Mauri Kostiainen

Advisors: PhD, Docent Veikko Linko
MSc Heini Ijäs

Author Iiris Hakaste

Title of thesis Förster resonance energy transfer analysis of a dynamic DNA origami nanocapsule

Degree Programme Life Science Technologies

Major Biosystems and Biomaterials Engineering

Thesis supervisor Professor Mauri Kostiainen

Thesis advisor(s) PhD, Docent Veikko Linko, MSc Heini Ijäs

Date 16.02.2019 **Number of pages** 7+62 **Language** English

The construction of nanostructures from DNA has proven as an ingenious approach to creating novel materials with a multitude of applications. An eminently robust method is the DNA origami folding technique, which allows the design of arbitrary structures that can be functionalized with nanometer precision and produced with high yields. The applicability of DNA origami is further expanded by the creation of dynamic structures that can be programmed to respond to various stimuli ranging from predefined DNA strands to external stimuli, such as pH.

In this thesis, the function of a pH-responsive dynamic DNA origami nanocapsule is characterized. The folding of the structure is assessed using agarose gel electrophoresis and transmission electron microscopy. The conformation of the nanocapsule is investigated with Förster resonance energy transfer (FRET) analysis of the profiles of the emission spectra of a FRET dye pair incorporated into the capsule at varying pHs. The dynamics of the conformational changes in the capsules were studied with kinetic fluorescence measurements, and the effect of sodium chloride and magnesium chloride on the process and the capsule structure were evaluated.

The results of this thesis suggest that the DNA origami nanocapsule is able to adopt both open and closed conformations as well as switch between these states in response to the environmental pH-stimuli. The kinetics and success of the conformational changes are significantly affected by magnesium chloride concentration. However, capsule conformation and structure are unaffected by exposure to physiological sodium chloride concentrations. Importantly, the pH-response (transition pH value) was found to agree with the prediction suggesting that the responsivity in these types of DNA origami structures can be rationally designed according to the application.

Keywords DNA nanotechnology, DNA origami, FRET, pH control

Tekijä Iiris Hakaste

Työn nimi Dynaamisen DNA-origami -nanokapselin Försterin resonanssienergiansiirtoanalyysi

Koulutusohjelma Life Science Technologies

Pääaine Biosystems and Biomaterials Engineering

Työn valvoja Professori Mauri Kostiainen

Työn ohjaajat FT, dosentti Veikko Linko, FM Heini Ijäs

Päivämäärä 16.02.2019 **Sivumäärä** 7+62 **Kieli** Englanti

DNA:n käyttö nanorakenteiden rakennusmateriaalina on osoittautunut nerokkaaksi strategiaksi luoda uudenlaisia materiaaleja lukuisiin sovelluksiin. DNA-origami -tekniikka on erityisen tehokas menetelmä, joka mahdollistaa monimutkaisten rakenteiden suunnittelun, verrattain korkean tuotantosaannon sekä suhteellisen helpon funktionalisoinnin nanometrien tarkkuudella. Mahdollisia käyttökohteita ovat entisestään lisänneet dynaamiset DNA-origamirakenteet, jotka voidaan ohjelmoida reagoimaan DNA-juosteiden sitoutumisen lisäksi erilaisiin ulkoisiin ärsykkeisiin, kuten ympäröivän liuoksen pH-arvoon.

Tässä diplomityössä karakterisoidaan dynaamisen DNA-origami -nanokapselin rakennetta ja vastetta erilaisiin pH-ympäristöihin. Tuotettuja origamirakenteita tutkittiin geelielektroforeesilla sekä läpäisyelektronimikroskopialla. Kapseleiden konformaatio eri pH-arvoissa karakterisoitiin hyödyntämällä Försterin resonanssienergiansiirtoon (FRET) perustuvaa analyysiä fluoresoivalla FRET-parilla leimattujen näytteiden emissiospektrien profiilista. Konformaatiomuutosten dynamiikkaa tutkittiin kineettisillä emissiomittauksilla, ja myös magnesiumkloridi- sekä natriumkloridikonsentraatioiden vaikutus prosessiin ja kapselin rakenteeseen arvioitiin.

Työn tulokset osoittivat DNA-origami nanokapselin omaksuvan sekä avoimen että suljetun konformaation sekä vaihtelevan näiden välillä ympäristön pH:n mukaan. Magnesiumkloridikonsentraatiolla huomattiin olevan mittava vaikutus onnistuneisiin kapselin konformaatiomuutoksiin sekä niiden kinetiikkaan. Sen sijaan edes fysiologisella natriumkloridikonsentraatiolla ei näyttänyt olevan vaikutusta kapselin konformaatioon tai rakenteeseen. Erityisesti kapselin pH-vasteen todettiin olevan ennustetun kaltainen, minkä perusteella näinkin kookkaiden DNA-origamirakenteiden responsiivisuus ulkoisiin ärsykkeisiin voidaan suunnitella sovelluskohteen mukaan.

Avainsanat DNA-nanoteknologia, DNA-origami, FRET, pH-kontrolli

Acknowledgements

This thesis work was conducted in Biohybrid Materials group at Aalto University in the School of Chemical Engineering. I would like to thank Mauri Kostiainen for the opportunity to join the group and for supervising my thesis. Especially I want to express my gratitude to my advisors Veikko Linko and Heini Ijäs for their guidance and valuable feedback throughout this project. I also want to thank Boxuan Shen for the TEM imaging. Special thanks go also to the whole group: even without all the cake and sweets working with you has been a joy.

As returning my thesis means finishing my Master's degree, I would also like to acknowledge the people and the community who have made my years in Aalto enjoyable. Additionally I want to thank the Chemistry Guild, V&V and Hankkijat for all the amazing times: without you, I would have graduated years ago. Above all, I want to thank my friends and family for their invaluable support and company throughout these years.

Espoo, February 16, 2019

Iiris Hakaste

Table of Contents

Symbols and abbreviations

Symbols

A	absorbance
c	concentration
I	fluorescence emission intensity
l	length of the light path
E	Förster resonance energy transfer efficiency
ε	extinction coefficient
τ	fluorescence emission lifetime
ϕ	quantum yield
λ	wavelength

Abbreviations

AFM	atomic force microscopy
AGE	agarose gel electrophoresis
aPCR	asymmetric polymerase chain reaction
B-DNA	B-form DNA
bp	base pair
cryo-EM	cryogenic electron microscopy
DNA	deoxyribonucleic acid
dsDNA	double-stranded DNA
DX	double-crossover
EDTA	ethylenediaminetetra acetic acid
EMSA	electrophoretic mobility shift assay
EtBr	ethidium bromide
FOB	folding buffer
FRET	Förster resonance energy transfer
MES	2-(*N*-morpholino)ethanesulfonic acid
$MgCl_2$	magnesium chloride
NaCl	sodium chloride
PEG	poly(ethylene glycol)
PCR	polymerase chain reaction

ssDNA	single-stranded DNA
TEM	transmission electron microscopy
Tris	tris(hydroxymethyl)aminomethane
UV/VIS	ultraviolet/visible (spectrophotometry)

1 Introduction

The conception of DNA as merely the genetic material has been revolutionized by the rapidly growing field of DNA nanotechnology. The wheels were set in motion by Nadrian ‘Ned’ Seeman in the 1980s [1] and have been accelerated especially ever since the invention of DNA origami in 2006 [2]. The exploitation of the selective hybridization and properties of DNA in creation of nanomaterials enables the design of arbitrary objects with highly predictable structures and endless possibilities for functionalization with the precision of nanometers. These attributes yield a multitude of applications ranging from nanophotonics to drug delivery.

In recent research increasing interest has been directed to dynamic DNA nanodevices that open up the field for even wider range of applications, e.g. drug nanocarriers that present their cargo in response to a specific clue [3]. Movement in these systems is induced in various ways, from which the use of strand displacement reactions is one of the most common strategies. However, the applicability of strand displacement reliant structures is restricted by the need of separate addition of a set of DNA strand ‘keys’. Thus their use in biological environments is quite challenging and inconvenient. More appealing approaches include the use of binding to cellular components (e.g. aptamers) or external stimuli (e.g. light, temperature, pH) to trigger the conformational change in the DNA nanodevice. Devices whose response to the stimuli can be rationally tuned are especially auspicious for functional applications. One example of such structures are pH-triggered systems that rely on DNA triple-helix formation.

In this thesis, the function of a pH-responsive dynamic DNA nanocapsule is characterized using Förster resonance energy transfer. The purpose is to demonstrate the functionality of the designed system in varying environmental conditions as well as obtain information on kinetics of the opening and closing mechanisms. Chapter 2 discusses the structure of DNA with emphasis on multistranded systems relevant for this thesis, and introduces the concept of DNA nanotechnology. Chapter 3 focuses on the design and production of DNA origami as well as a discussion of dynamic DNA origami systems. Chapter 4 covers the Förster resonance energy transfer phenomenon, use in probing dynamic DNA origami function and methods for quantification of energy transfer efficiency. Materials and methods used in this thesis are covered in Chapter 5, and the results obtained them presented and discussed in Chapter 6.

2 Deoxyribonucleic acid

The interest in deoxyribonucleic acid (DNA) was high already in the 1940s, when biologists were trying to comprehend how this molecule with a simple seeming chemical composition could be responsible for carrying all genetic information [4]. It was only the discovery of the double-helical structure of DNA [5–7] in 1953 that elucidated the capability of this molecule to store information and convey it onward in the process of cell replication. From these same foundations in the 1980s arose the idea of DNA nanotechnology: a field that continues growing exponentially to this day.

2.1 The structure of DNA

There are four bases present in DNA: adenine (A), thymine (T), cytosine (C) and guanine (G) which belong to two classes: monocyclic pyrimidines (C and T) and bicyclic purines (A and G). A base bound to a 2'-deoxy-D-ribose is called a nucleoside and esterifying a phosphate to the 5' carbon of the ribose yields a nucleotide. Nucleotides are the building blocks of DNA: joining a 5' phosphate group of a nucleotide to the 3' hydroxyl group of the next nucleotide with a phosphodiester linkage creates a strand of DNA (Figure 2.1). When two antiparallel DNA strands are joined together via hydrogen bonding between the bases of the nucleotides, a DNA double helix is formed. This phenomenon is referred to as Watson-Crick base pairing, which is highly regulated: cytosine will bind only with guanine forming three hydrogen bonds and adenine only with thymine via two hydrogen bonds. This means that two single-stranded DNA molecules (ssDNA) will bind together to form a double helix (dsDNA) only if their base sequences are complementary to each other. [8]

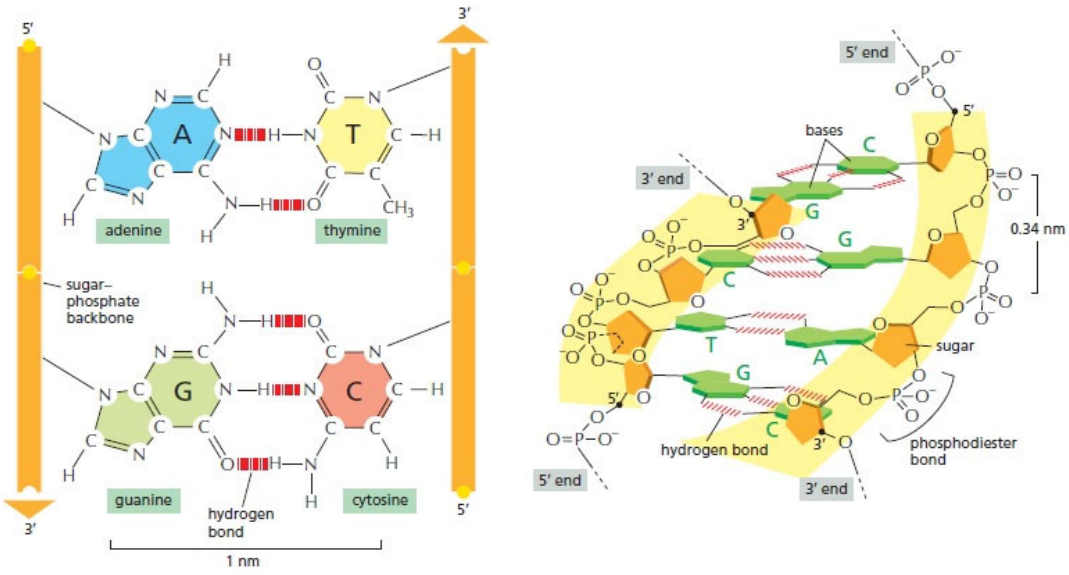

Figure 2.1: Structure of DNA. Hydrogen bonds between Watson-Crick base pairs adenine (A) - thymine (T) and guanine (G) - cytosine (C) and the composition of the sugar-phosphate backbone. [4]

In addition to Watson-Crick hydrogen bonds that hold the DNA double-helix together, the helical structure is also stabilized by base-stacking interactions and hydrophobic effects. In the inside of the helix, base pairs are stacked on top of one another. This proximity induces attraction between base pairs due to pi-stacking of the aromatic rings bringing a substantial stabilizing net effect due to the amount of interactions in one DNA molecule, even though the energy in a single interaction is quite small. DNA double helix is also stabilized by the hydrophobic effect: the polar sugar-phosphate backbone is facing outwards as the hydrophobic bases stack inside the molecule. These stabilizing forces in physiological conditions yield a DNA double-helix with 3.4 Å between base pairs, right-handed helix with diameter of 20 Å and 10.5 bases per full helical turn. This structure is also referred to as B-form DNA. [9–11]

The DNA double helix can adopt other forms as well in addition to B-form: two well-characterized examples are A-form and Z-form DNA (Figure 2.2). A-form DNA is often found in environments with low humidity and high salt concentrations. It is more densely packed with 11 base pairs per helical turn widening the helix diameter to about 26 Å and resulting in a 2.6 Å helix rise per base pair, and the base pairs are tilted 20º in relation to the helical axis. In addition to the right-handed helices also left-handed forms are possible, such as Z-form DNA. It is a product of alterations in the

glycosylic bonds in the nucleotides between the base and the deoxyribose. In A-form and B-form DNA, all glycosylic bonds are in anti-conformation, but in Z-form DNA, purine-containing nucleotides have glycosylic bonds in syn-conformation. This results in a zigzag appearance of the sugar-phosphate backbone and further causes the left-handed twist of the helix. In Z-form DNA, there are 12 base pairs per helical turn and 3.7 Å helix rise per base pair. Also Z-form DNA is stabilized by high salt concentrations, and changing the environmental conditions can cause a DNA molecule to alternate between the different forms. [8, 12]

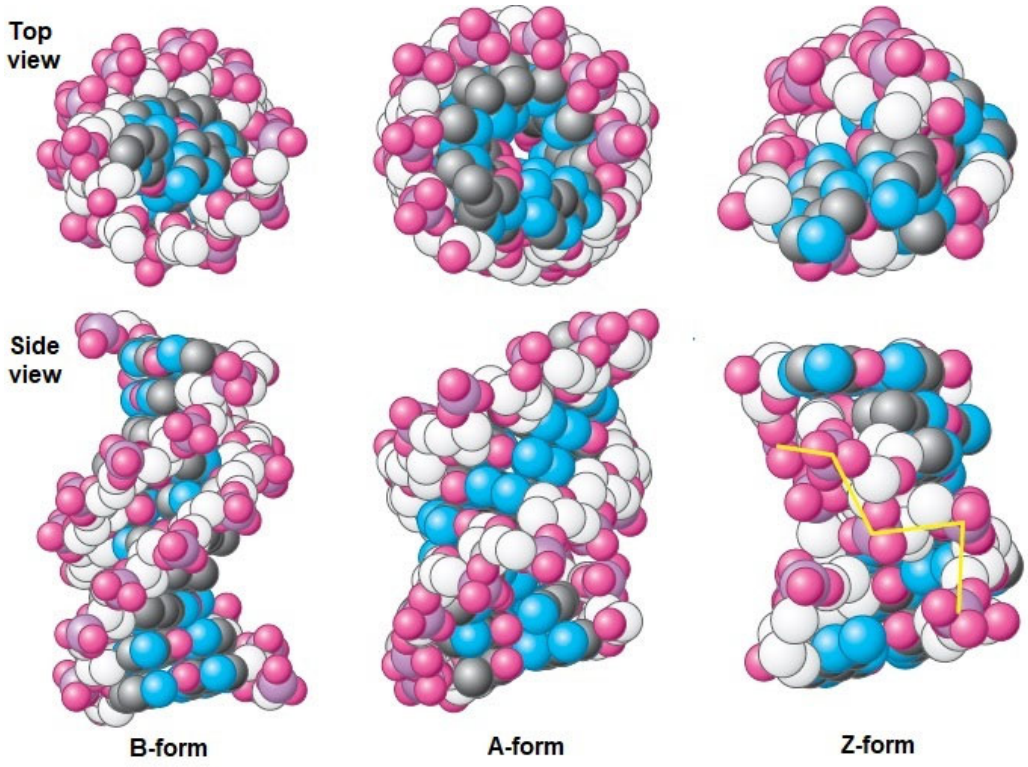

Figure 2.2: Different forms of DNA. Models of 10 base pairs of DNA in B-form, A-form and Z-form. Adapted from [9]

2.2 Multistranded DNA structures

Depending on the strand sequence and surrounding conditions DNA can also form structures with more than two strands. Watson-Crick base paired nucleotides still have potential hydrogen bonding residues available, especially in the double-helix

major groove side, referred to as the Hoogsten face. Using them to form additional hydrogen bonds (referred to as Hoogsten base pairing or Hoogsten interactions) yields multistranded structures, such as triplexes and tetraplexes. [12] In the scope of this thesis, the focus is mostly on the formation and properties of triplex systems, nevertheless tetraplexes are briefly discussed.

Tetraplexes can form between strands that have guanosine- or cytosine-rich areas: four G-rich strands form a G-tetraplex (often referred to as the G-quadruplex) and C-rich strands an intercalation motif (i-motif). Even though both are four-stranded, the structures are fundamentally different. In G-quadruplex, one G-tetrad has four guanosines in a ring that each have formed two hydrogen bonds form the Watson-Crick face and two form the Hoogsten face to the adjacent guanosines (Figure 2.3 a). This way they are nearly co-planar, and the structure is further stabilized by stacking interactions between the G-tetrad layers on top of each other. G-quadruplex is stable at neutral pH, whereas the formation of a cytosine-rich i-motif requires the protonation of half of the Cs. Then a C^+ can form three hydrogen bonds with an unprotonated C (Figure 2.3 b), and the two formed parallel C^+•C –duplexes are intercalated together: hence the name i-motif (Figure 2.3 c). The i-motifs are only stable at pH values below 7 with the highest stability around the pK_a of cytosine (4.6 in pure water at 25ºC). [12, 13]

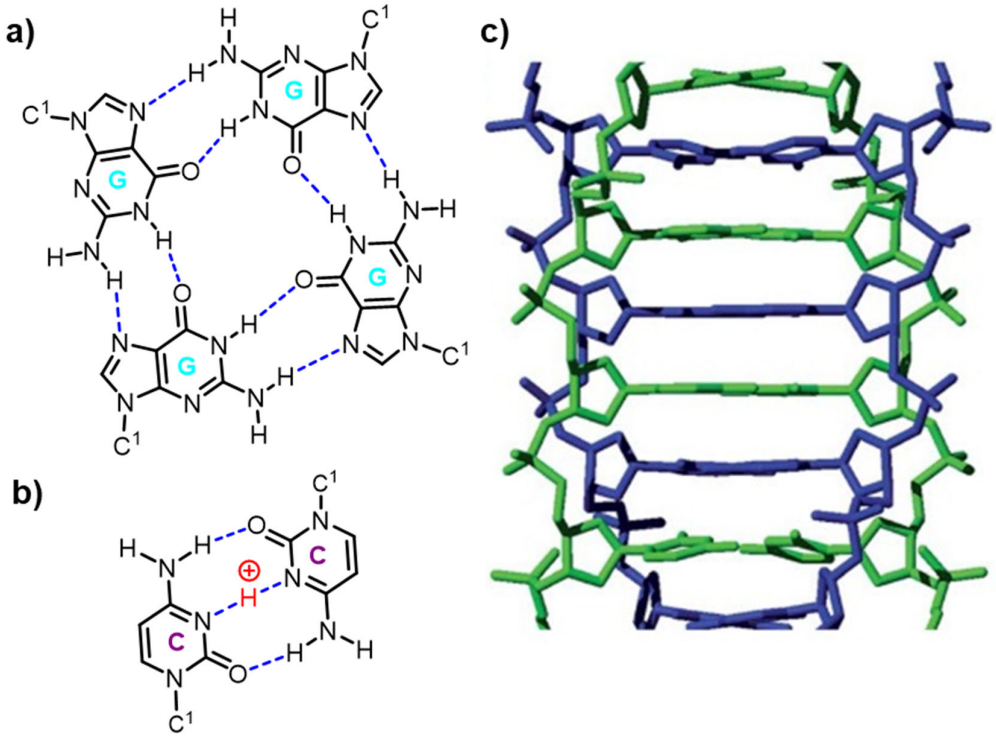

Figure 2.3: a) Hydrogen bonding in a G-tetrad. b) Hydrogen bonding between two cytosines in an i-motif. c) Intercalated structure of an i-motif. c) adapted from [13].

In DNA triplex formation a third ssDNA binds to the major groove of a dsDNA via Hoogsten base pairing (Figure 2.4). Similarly as in Watson-Crick base pairing, Hoogsten interactions are specific: thymidine can pair with adenosine in an A-T pair (T•A-T, Figure 2.4) and protonated cytidine (C^+) with guanosine in a G-C pair, thus C^+•G-C bonding is dependent on acidic conditions. As a result, the whole triple-helix is more stable at low pH. The triplex formation relies on the chemical composition of the participating strands. In this case, the double-helix is formed of a homo-purine and homo-pyrimidine strand, and the third strand that binds with parallel via Hoogsten base pairs to the purine strand is also a homo-pyrimidine. It is also possible that the third strand is instead a homo-purine, in which case it binds anti-parallel and the base triples are G•G-C and A•A-T formed via 'reverse' Hoogsten interactions (Figure 2.4). As a rule, the third strand binds anti-parallel to the chemically homologous strand in the double-helix. [8] Absolute strand homology is not required for triplex formation, as interruptions are tolerated by third strands containing the analogous changes. Triplex formation can be intermolecular or intramolecular. [14]

Even though the DNA triplex can form with the help of Hoogsten (parallel third strand) or reverse Hoogsten (antiparallel third strand) interactions, the parallel binding is most often exploited in applications. This is due to the better stability of the Hoogsten base paired triple helix over the reverse Hoogsten base paired. This is caused by several factors, such as that Hoogsten base paired triples are structurally isomorphic in regard of the C^1 position, as seen in Figure 2.4. This results in minimal distortion of all helices involved in the triplex: studies show that the double-helix structure only shifts slightly towards A-type DNA rather than B-DNA. Another thing to consider is that reverse Hoogsten base triple formation requires a guanosine-rich third strand. Those can be prone to form G-quadruplex structures which evidently do not facilitate triple-helix formation. Another noteworthy observation is that the formation of Hoogsten triplet C-G•C^+ requires the protonation of the third strand cytosine, whereas reverse Hoogsten triplet does not. The additional hydrogen ion can in fact assist in the triple-helix stabilization by screening the electrostatic repulsion between the negatively charged DNA strands. [14]

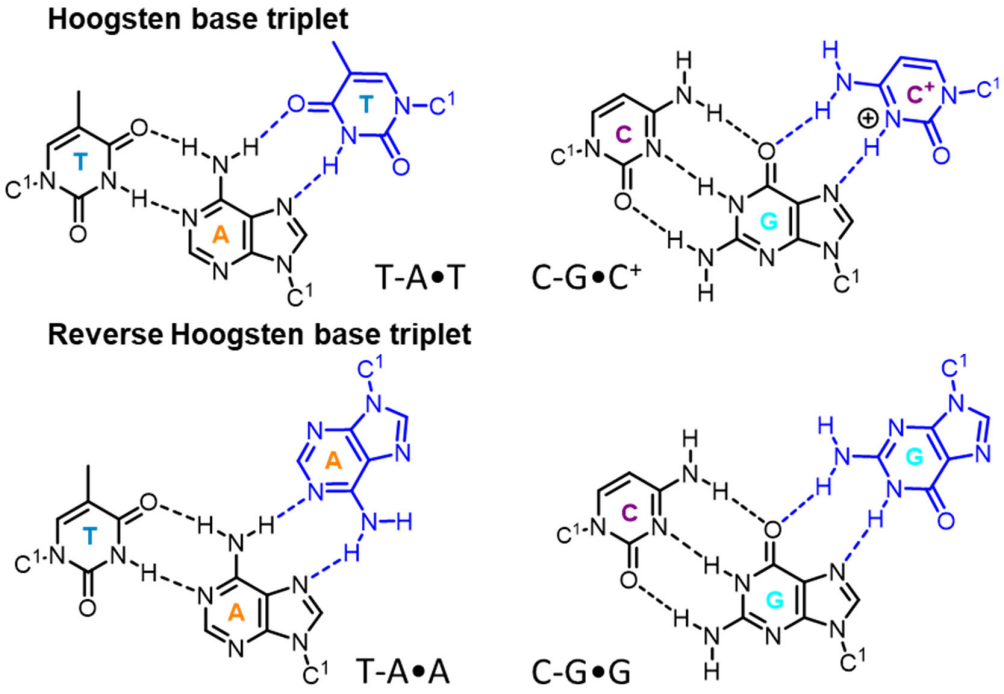

Figure 2.4: Hoogsten and reverse Hoogsten base triplets. The Watson-Crick base pair and hydrogen bonds with black, the third strand base and Hoogsten interactions with blue.

The effect of protonated cytosines is not always stabilizing, as too many consecutive cytosine residues can have the opposite effect. The ideal stability is achieved with alternating between regions of the two triplets [15]. Shifting the relation of C-G•C^+ and T-A•T regions in the sequence results in triplets that assemble at varying pHs, and this programmability is a significant advantage over the previously discussed i-motif. There are also strategies for improving the binding affinity of the third strand, such as increasing length, conjugating triplex-stabilizing ligands or increasing the cation concentration (most often with divalent ions such as magnesium Mg^{2+}). Some mismatches in the third strand or duplex can also be tolerated: the further away from the center of the sequence, the less it destabilizes the triplex. Due to the quite robust formation and the vast tuning possibilities, triple-helixes can readily be exploited for the purpose of dozens of applications [16]. [14] The pH response programmability is the most important quality for this thesis, and is further discussed in the context of use in DNA nanotechnology in Chapter 3.3.

2.3 DNA nanotechnology

As the information of DNA molecule's unique structural properties and their function dawned on the world, the arena was open for ideas on how to use them. In the beginning of 1980s, N. C. Seeman came forward with the idea of creating a DNA lattice that would allow the arbitrary and accurate design of artificial crystals [17]. This was the spark for the creation of the field of DNA nanotechnology [18, 19]: a field set on controlling the spatial and temporal arrangement of matter in a nanometer scale made possible by the properties of the DNA molecule. DNA nanotechnology is built on three pillars: the selective and efficient hybridization of DNA, the design of immobile and branched junctions and the advanced technologies to synthetize custom DNA sequences. [20]

The properties of DNA covered in chapter 2.1 provide basic understanding of the selectivity and efficiency of DNA double-helix formation for the requirements of DNA nanotechnology, but the hybridization of two double-stranded DNA molecules via sticky ends [21] is a necessary addition. Sticky end hybridization follows the same Watson-Crick base pairing rules and is thus highly selective allowing the prediction of not only the components of the assembly reaction but also the product structure [20, 22]. Similarly, branched junctions are possible due to the structural properties of DNA

and occur naturally in various states of the cell cycle, such as in a replication fork and in a four-arm Holliday junction [23]. However, these junctions are naturally mobile due to the sequence complementarities and are thus unstable, which is why the immobility of the structures can be achieved only with specifically designed strand sequences [24]. Thus we arrive at the third pillar of DNA nanotechnology: the requirement of DNA sequence synthesis. DNA strands with arbitrary sequences can nowadays be purchased from several biotechnology companies, and new production method has also been recently developed [25].

Building on these foundations and starting with the design [1] and creation of an immobile four-branched junction [26] Seeman's group also demonstrated the conceptual idea of creation of DNA nanocrystals via sticky end cohesion of branched building blocks (Figure 2.5 a). This goal was achieved [27] using double-crossover (DX, Figure 2.5 b) motifs [28] as building blocks, which were able to provide the required rigidity for a stable structure that the more flexible branched junctions lacked [29]. Seeman's group went on to create first triple crossovers (TX) [30] and then paranemic crossovers (PX) [31] with its topoisomer JX_2, which were then used in a simple nanomechanical device [32]. The DX, PX and JX_2 became important motifs to be used frequently in DNA nanotechnology to create increasingly complicated lattices in two (2D) and even three dimensions (3D). These methods contained a few impracticalities regarding the precise stoichiometric requirements in the self-assembly process and the lack of control over the final structure size, for which the invention of the DNA origami method [2] provided an attractive option. [18] DNA origami will be the main focus of chapter 3.

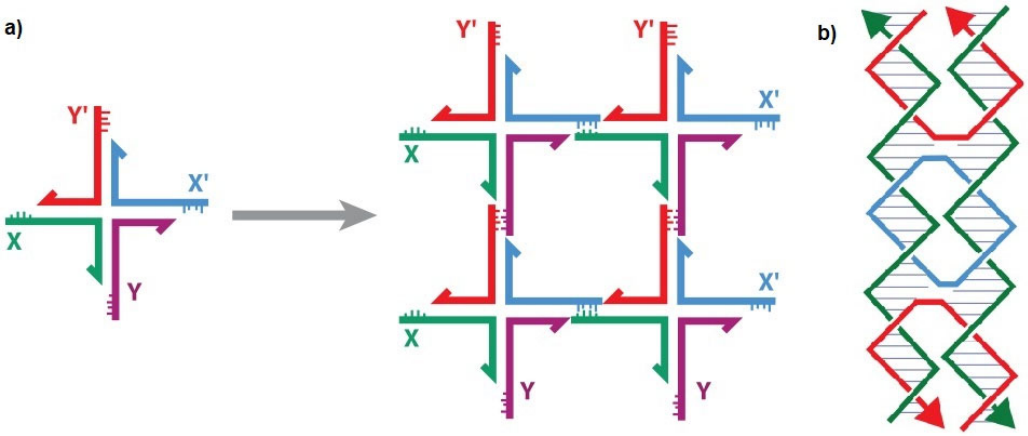

Figure 2.5: a) Four-arm immobile DNA motifs with sticky-ends can be combined to yield a 2D-lattice. b) Double-crossover (DX) tile. Adapted from [20].

3 DNA origami

Paul Rothemund's invention of the DNA origami method [2] was a significant leap toward the enabled state of DNA nanotechnology [33]. This highly robust method is built on the aforementioned molecular and structural properties of the DNA molecule especially taking advantage of the intrinsic and selective binding between two DNA strands. In DNA origami method one long single-stranded DNA molecule, a 'scaffold', is folded with the help of dozens of small binding DNA strands, 'staples', which results in the target structure formation. By meticulously designing the staple sequences virtually any structure can be produced. These structures can be further decorated with any material that can be conjugated into DNA, which yields organized functionalities at a nanometer level [34]. The arbitrary nanoscale design, robustness and plentitude of possible structural variations make DNA origami an extraordinarily powerful method with vast number of possible applications [35, 36]. The abundance of applications is covered in an extensive pool of publications, including but not limited to reviews on drug delivery [37–39] and other biomedical applications [40], enzyme reactors [41], DNA walkers and nanomachines [42, 43] photonics [44] and plasmonics [45, 46] (Figure 3.1).

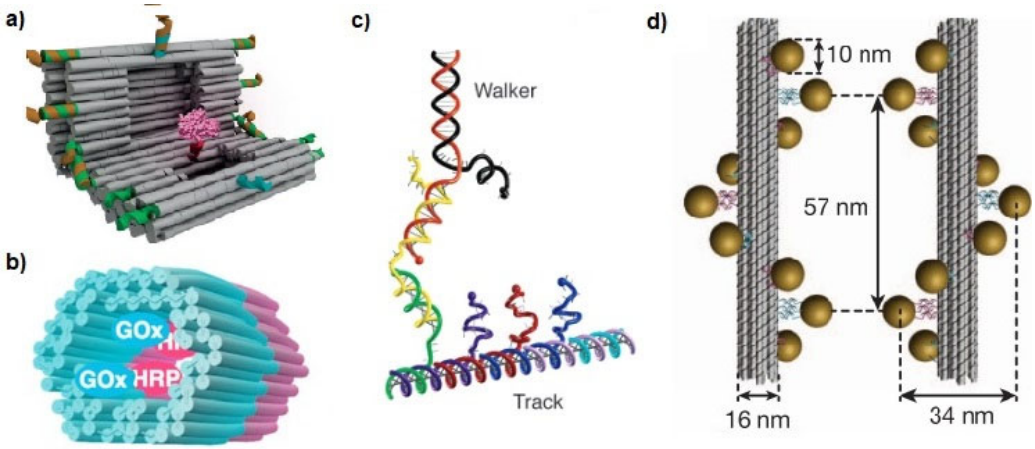

Figure 3.1: Applications of DNA origami. a) Reconfigurable nanovault with strand displacement locks for enzyme encapsulation [47]. b) DNA-origami based enzyme cascade nanoreactor [48]. c) A DNA walker [49]. d) DNA origami and gold nanoparticle plasmonic structure [50].

3.1 Basic principles of DNA origami design

The first step in the structure design of a conventional DNA origami is to create a model of the desired structure using parallel cylinders as building blocks to represent the forthcoming double-helix (Figure 3.2). The chosen scaffold is then routed through this model in a way that covers each position once and thus forms the other half of each double helix motif. The motifs will be completed by adding short staple strands that usually run through more than one helix switching from one helix to the adjacent one in positions referred to as crossovers. [2] In other words, DNA origamis can be said to be formed of multiple DX-motifs (presented in Chapter 2.2) that have one long strand running through all of them [51].

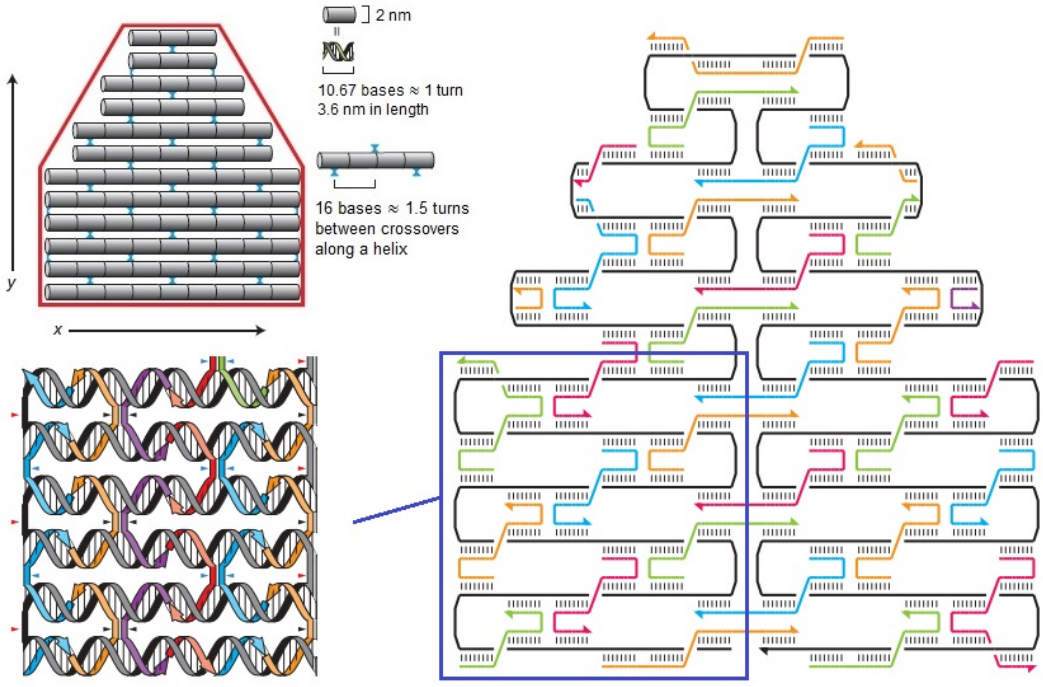

Figure 3.2: Principles of 2D DNA origami design. Top left is the cylinder representation of the structure. Scaffold and staple strand routings shown on the right: staple strands form most of the crossovers. Double-helix representation of the structure showing the crossovers illustrates the appropriate position of the DNA strand backbone. Adapted from [2].

Crossovers can be formed in positions where the strand backbone is in a suitable position when moving to the adjacent double-helix motif (Figure 3.2 d). Thus the ideal position of crossovers in an origami structure depends on the used type of packing lattice as well as the desire to create twists or bends. In his original work, Rothemund designed 2D origamis on a square lattice, where each helix has two neighboring helices on opposite sides. This means that the spacing of crossovers in the same side of the helix should ideally be a factor of full-turns and crossovers to alternating sides a factor of half-turns of the helix in order to arrive to a suitable crossover position. The spacing of crossovers on a square lattice affects the interhelical gap: in this type of parallel arrangement the helices tend to bend out due to electrostatic repulsion. Using crossovers to alternating sides of the helices with spacing of 1.5 helical turns resulted in an interhelical gap of 1 nm, whereas increasing the spacing to 2.5 helical turns yielded a 1.5 nm gap. [2] The 1.5 helical turns between crossovers in Rothemund's design meant 16 bps, which equals to 10.67 bp per one full helical turn. Exceeding the 10.5 bp per turn typical for B-DNA (discussed in chapter 2.1) causes strain on the structure and leads to global right-handed twisting [35]. This twisting combined to the relatively flexible structure of single-layered DNA origami can be exploited to create curved 2D structures [52, 53].

2D origami layers can be used to construct hollow 3D objects [54], but creating space-filling 3D structures requires using multilayer DNA origami design techniques. For this, a square lattice [55], a honeycomb lattice [56], a hexagonal lattice or a hybrid of these [57] can be used, which all have different crossover rules. For example on a square lattice there are up to four possible crossover directions to a neighboring helix, but on a honeycomb lattice there are three (Figure 3.3 a). B-DNA does a full 360º turn in 10.5 bp, which equals to 240º rotation per 7 bp. Thus the crossovers in a honeycomb lattice have to be placed with 7 bp intervals to the three neighboring helices with 21 bps between crossovers to the same neighboring helix (Figure 3.3 b). By deviating from this 7 bp spacing rule by adding or removing bases between crossovers, local twist can be introduced to the structure (Figure 3.3 c). This can be used in rational design to create structures with curves and twists [58]. Spacing crossovers in square lattice with four helical neighbors is not as straightforward: 21 bp spacing between crossovers to the same neighbor helix would indicate 5.25 bp average spacing between crossovers to the remaining three neighbors. Thus the crossover spacing interval has to be irregular in order to avoid twisting of the structure. [59]

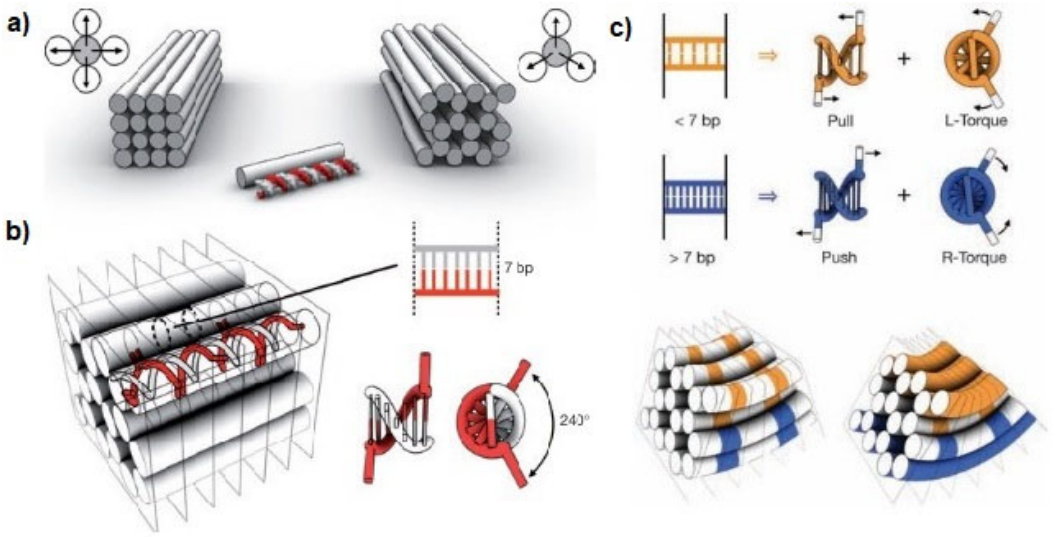

Figure 3.3: Design of 3D DNA origami. a) Illustrations of square and honeycomb lattices with the possible crossover directions. b) Crossover spacing in honeycomb lattice. a) and b) adapted from [59]. c) The strain caused by deviating from 7 bp interval between crossovers causes the structure to bend. Adapted from [58]

Designing DNA origami structures and staple sequences by hand would be a laborious task, as would the prediction of the structure of the designed origami. Therefore computational methods have been created to aid with the design and modelling of DNA origami structures. An open-source software package caDNAno [60] enables efficient design of both 2D and 3D origami structures using either square or honeycomb lattice. The software enables automated staple design and exports a list of the staple strand sequences based on the scaffold chosen by the user. These design files can be imported into structure modeling softwares such as CanDo [59, 61] or the structure prediction tool from Aksimentiev Group [62]. However, the scaffold routing has to be done manually in caDNAno, but is automated in lattice-free design softwares vHelix [63] and DAEDALUS [64]. They allow the top-down design of meshed DNA origami structures. Entirely scaffold-free methods also exist for the creation of 2D- and 3D-objects, such as DNA bricks [65].

There are many tuning possibilities in the origami design that can solve issues or bring new functionality to the structure. One common problem with DNA origami in solution is unspecific aggregation of structures due to the blunt-end stacking at the helical interfaces between objects (Figure 3.4 a). Aggregation can be reduced by lowering

the concentration of divalent cations (Mg^{2+}) in the solution after folding. However, a more efficient strategy is to design the origami structure with poly-T loops or tails in the helical ends (Figure 3.4 b). Thus there are no blunt ends and the aggregation of the structures can be significantly reduced. Single-stranded staple or scaffold loops can also be used to induce specific hybridization of individual DNA origami structures into higher-order assemblies (Figure 3.4 c). They can also be created through the aforementioned blunt-end stacking, which is directed into favorable positions through structure shape complementarity [66, 67]. Origamis can also be designed to have single-stranded staple portions protruding out from the structure surface, to which DNA-tagged components can be attached via strand hybridization. Thus spatially accurate functionalization of origami with proteins, metal nanoparticles etc. becomes feasible. Other strategy is to incorporate chemically modified staple strands to the structure, to which e.g. proteins can directly bind (for example streptavidin binding to biotin modified staple strand). [68]

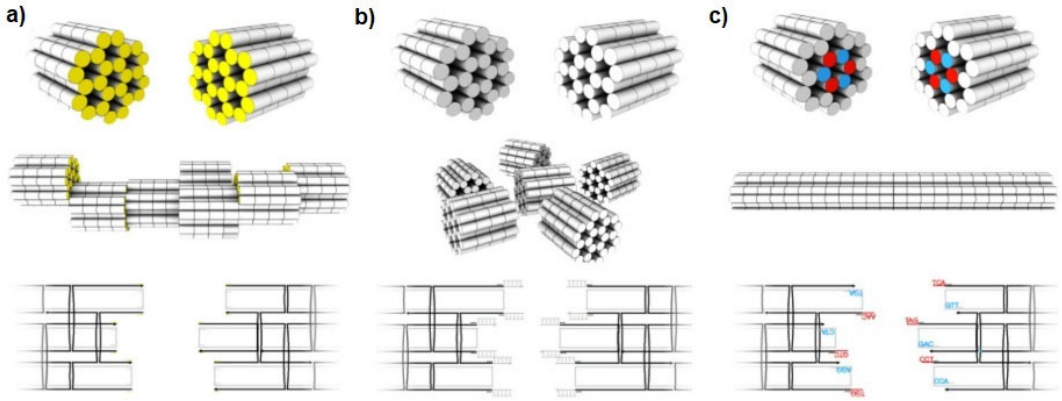

Figure 3.4: Stacking of 3D DNA origami structures. Illustrations show the structure and the aggregate formation, on the bottom the design scheme from caDNAno. a) Unspecific aggregation of structures due to blunt-end (yellow) stacking. b) The addition of poly-T tails (grey overhangs on the caDNAno scheme) on the ends of the structure reduces aggregation. c) Addition of complementary sticky-end overhangs to the ends of the structure yields an organized superstructure. Adapted from [67].

3.2 Production of DNA origami

The next step after designing the scaffold and staple routings for the desired DNA origami target shape (steps 1 and 2 in Figure 3.5) is to obtain the required scaffold

and staple strands. The naturally single-stranded genome of the bacteriophage M13mp18 (and its slightly varied versions) is the most commonly used scaffold strand with the length of 7249 nucleotides. Since the length of the scaffold is the limiting factor in the size of the DNA origami structure, scaffolds with varying lengths may be required for specific purposes. Various methods exist for the production of arbitrary scaffold strands, such as polymerase chain reaction (PCR) [69, 70] and asymmetric PCR (aPCR) [64], but scaffolds derived from phage genomes [56, 71] dominate the commercial product field [67]. There has also been interest in producing smaller scaffolds [72], using a double-stranded source of scaffold [73] and even the biotechnological mass production of DNA origami [25].

The number of required staple strands depends on the size of the scaffold strand and the length of the used staples. For example, commonly the folding of the M13mp18 scaffold requires around 200 staples [2]. To achieve high yields, staple strands are used in excess over the scaffold, but the exact stoichiometric ratios are not important. This is due to the preference of staple strands to hybridize with the scaffold rather than with each other, and that the advancing correct alignment of the structure promotes additional binding of correct staples. This also results in replacement of the incorrectly bound staples by correctly binding ones via strand invasion and other exchange mechanisms. Thus even the purity of the staple strand solutions is not that critical factor in correct structure folding, which demonstrates the robustness of the origami method. [68]

The scaffold and staples are mixed in a one-pot reaction with a buffer solution (usually Tris, acetic acid and EDTA in pH 8) with added divalent magnesium ions (Mg^{2+}). The solution is first heated sufficiently to denature all DNA strands, and slowly cooling the reaction to room temperature results to annealing of the scaffold and staple strands to produce the designed structure. This “folding program” is performed with a thermal cycler. The addition of positively charged Mg^{2+} ions is needed to screen the electrostatic repulsion between negatively charged DNA molecules. [2, 51] For some time the presence of magnesium ions was thought to be absolutely essential for the integrity of DNA origamis, but it is possible to fold origamis also in the presence of monovalent sodium ions [74]. Additionally, structures that have been folded in the presence of Mg^{2+} can retain their structural stability in suitable conditions even if the divalent cations are depleted from the solution after the folding process [75].

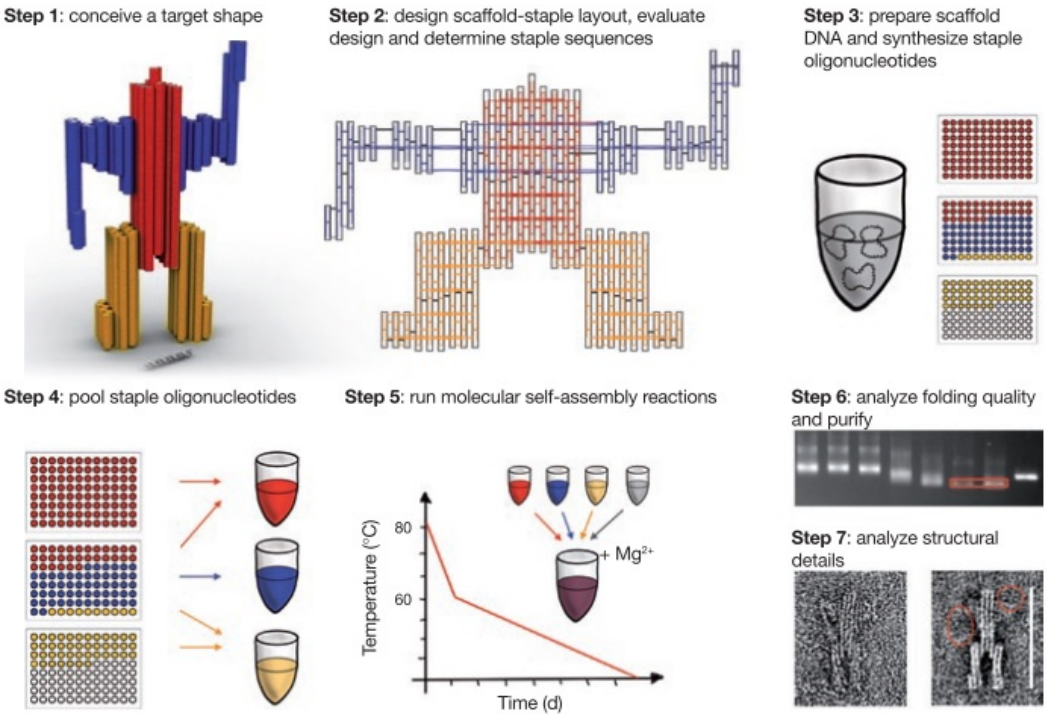

Figure 3.5: Production of DNA origami. Production starts with the design of the DNA origami structure: conceiving the target shape, routing the scaffold and staples and exporting the sequences. After obtaining the materials, staples can be pooled according to position in the structure to simplify possible required changes. After running the self-assembly reaction (duration can range from tens of minutes to days) folded structures are analyzed to determine quality, purity and structural details. [59]

After folding the origami structure solutions can be purified from excess staple strands. Multiple purification methods are available, such as poly(ethylene glycol) (PEG) purification [76], agarose gel extraction [56], rate-zonal centrifugation [77] and spin filtering [78]. There are also methods optimized especially for functionalized DNA origami structures, such as magnetic bead capture and fast protein liquid chromatography [79]. The success of the purification and the quality of the folded origami can be investigated with agarose gel electrophoresis (AGE). Imaging methods such as atomic force spectroscopy (AFM), transmission electron microscopy (TEM) and cryogenic electron microscopy (cryo-EM) [54, 80] are also used to gain information of the details of the structure.

3.3 Dynamic DNA origami systems

Even though the building of arbitrary and static 2D and 3D shapes with nanometer scale precision was a novel technique, the true potential for applications lies in the dynamic systems, which harness the DNA origami technique into creating multipurpose nanoscale devices. There are multiple ways to induce movement in these systems; some of the early examples even before the origami technique include exploiting the B-Z transition of DNA [81] and DNA hybridization with strand displacement [82] to create small nanomechanical devices. These same techniques are still used in larger scale devices. In addition to DNA-DNA interactions, dynamics is based on other molecular interactions with DNA and several experimental factors (such as pH, temperature, light) as discussed in the recent review [3]. In the scope of this thesis, the main focus is on pH responsive DNA origami systems, but also other stimuli-dependent drug encapsulation and delivery systems are explored.

As introduced in Chapter 2.2, the DNA triple-helix formation occurs due to pH-dependent Hoogsten interactions. Since the requirements for pH are different for C^+•G-C and T•A-T pairs, the preferred binding window for a specific DNA triplet can be chosen by modifying the sequences. This was demonstrated by Idili *et al.* [83], who created a programmable pH-triggered DNA nanoswitch (Figure 3.6). They showed that the pH window for the switch response varied with changes in the relative T•A-T concentration in the switch sequence. This was later used to create reconfigurable chiral plasmonic metamolecules assembled with DNA origami [84], whose conformation was controlled with pH-responsive locks. Multiple triple-helix motifs with different pH-windows can also be incorporated to achieve multiple conformations in one DNA nanostructure [85] or isomerization of smaller structures [86].

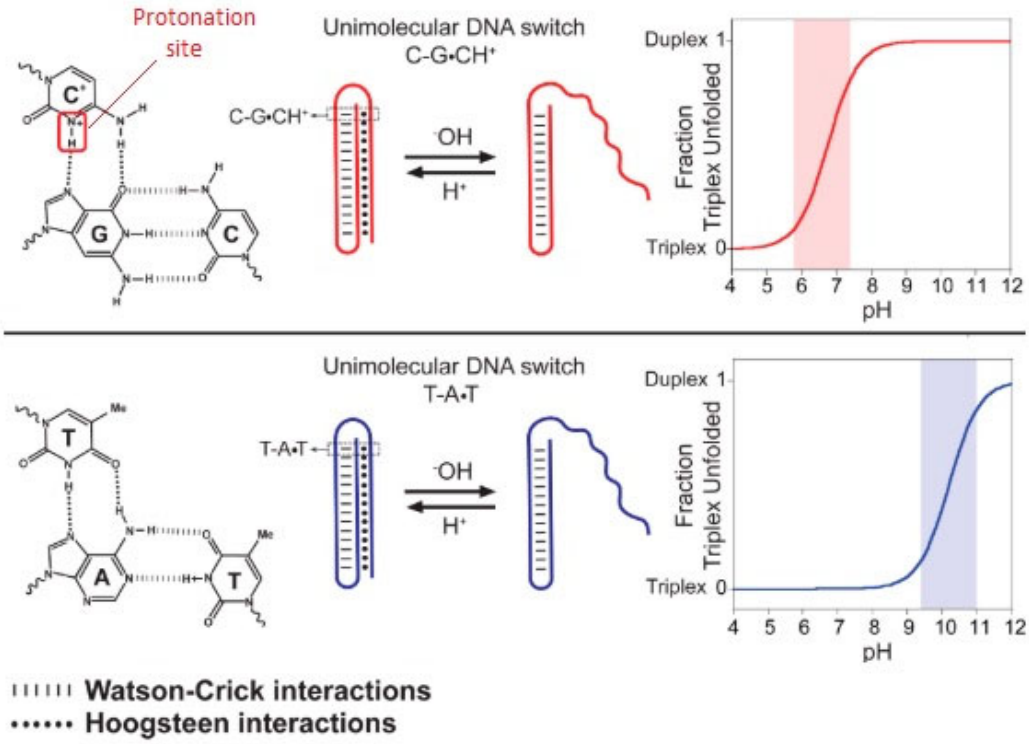

Figure 3.6: The pH-triggered DNA nanoswitch. As the formation of C^+•G-C triplet requires the protonation of the cytosines in the third strand (protonation site highlighted), the triplet switch (red) is only closed at lower pH ($pK_a \approx 6.5$). The T•A-T triplet is stable at a wider pH range, and the switch (blue) opens only after the deprotonation of thymine at higher pH ($pK_a \approx 10$). [83]

Even though the pH-responsive DNA triple-helix switch has applications due to its simplicity [16], a truly interesting approach is the incorporation of said switches into larger DNA nanostructures. This way dynamic systems can be created that would ideally be able to encapsulate functional enzymes and release them in response to environment pH. Indeed Ottaviani *et al.* [87] managed to engineer an octahedral DNA nanostructure with the pH-switch (Figure 3.7 a), that could be cycled between the open and closed states. More advanced encapsulation examples were created by Kim *et al.* [88] and Burns *et al.* [89] with a DNA tetrahedron cage regulating the function and accessibility of an enzyme and a DNA box with a lid loaded with green fluorescent protein, respectively. However, in both of these examples the pH-responsivity is obtained by exploiting i-motifs. Although functional, the use of i-motifs does not enable the fine-tuning of the pH-response region as triple-helix switches do.

Multitude of dynamic encapsulation devices exist that respond to stimuli other than pH. The first box with a lid was published already in 2009 [54], and the movement of the lid was controlled by strand displacement locks. The lid could be opened by adding specific ssDNAs referred to as keys (Figure 3.7 b). The strand displacement lock system is yet quite recently used in a more complex system by Grossi *et al*. [47], creating a nanovault (Figure 3.1 a) that can be cycled between states with the help of opening and closing keys, and is shown to encapsulate an enzyme. Strand displacement lock examples are well functioning, yet it is difficult to see their potential in *in vivo* drug delivery applications since the opening requires the introduction of the keys as well. A more feasible approach would be the use of DNA-aptamer locks that open due to protein displacement [78]. These can be designed to respond to e.g. specific cell surface proteins. Development of encapsulation systems responding to entirely external stimuli still remains appealing; e.g. a photoresponsive DNA nanocapsule (Figure 3.7 c) has been created [90].

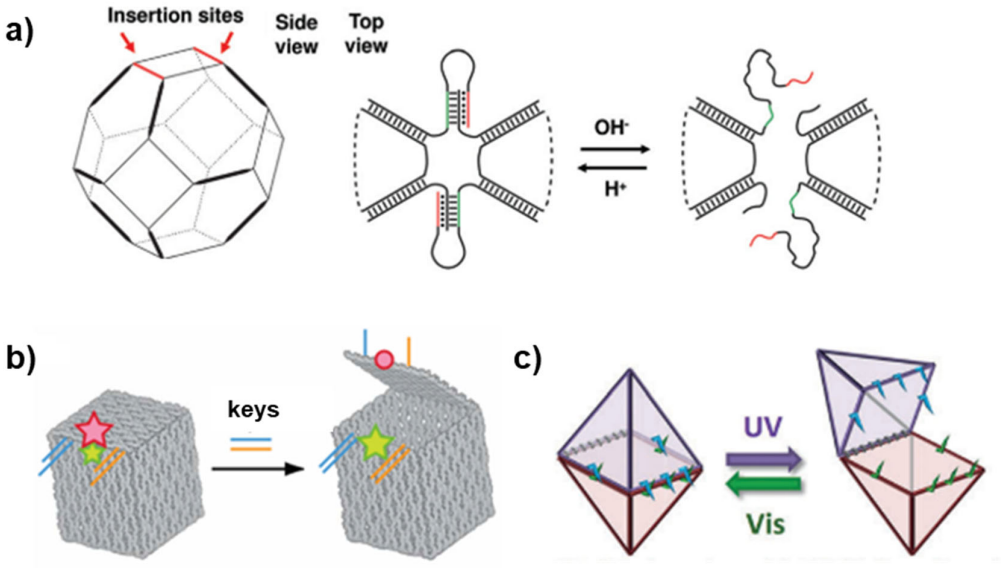

Figure 3.7: Examples of dynamic DNA origami systems responding to different stimuli. a) pH-responsive octahedral DNA nanocage that uses triplex DNA motifs. Adapted from [87]. b) DNA origami box with a lid opened by addition of strand displacement keys. Adapted from [54]. c) Photoresponsive DNA origami nanocapsule that can be cycled between open and closed states with UV and Vis light. Adapted from [90].

4 Förster resonance energy transfer

Förster resonance energy transfer (FRET), also referred to as fluorescence resonance energy transfer is a phenomenon in which two particles interact: a donor in an electronically excited state (D*) and an acceptor in a ground state (A). Energy is transferred non-radiatively from donor to acceptor (without the appearance of a photon), and is based on dipole-dipole interactions. The transfer of energy causes the donor to return to ground state and promotes the acceptor to an excited state. If the acceptor is a fluorescent molecule, it can then return to the ground state through emission of a photon. In this case, FRET can be detected as a decrease in donor emission and increase of acceptor emission. The acceptor can also relax non-radiatively and is then referred to as a quencher. In this case, energy transfer is detected only as a decrease in donor emission. FRET requires overlap of the emission spectrum of the donor and absorption spectrum of the acceptor (Figure 4.1). In addition to the extent of the spectral overlap, the efficiency of the energy transfer relies on the relative orientation of the dipoles, quantum yield of the donor and most importantly, the distance between the donor and acceptor. [91, 92]

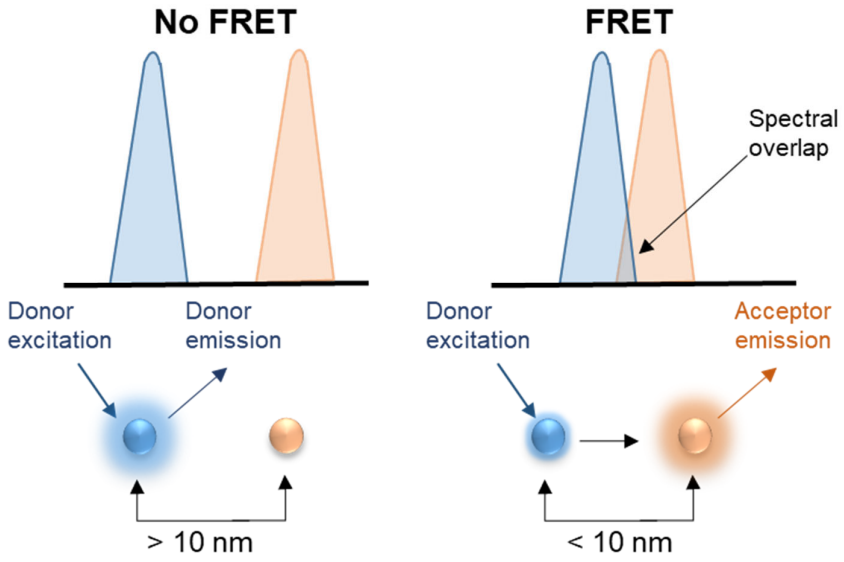

Figure 4.1: Top panel shows donor emission (blue) and acceptor absorption (orange) spectra that have to overlap for the FRET to occur. Bottom panel illustrates the significance of the distance between donor and acceptor fluorophores. When they are located sufficiently close (<10 nm), FRET can be detected as decrease in donor emission intensity and increase in acceptor emission intensity upon donor excitation.

The correlation between donor and acceptor distance and the efficiency of FRET is strong: the efficiency *E* is defined as

$$E = \frac{R_0^6}{r^6 + R_0^6} \tag{4.1}$$

where *r* is the distance between the donor and the acceptor and R_0 is the Förster distance: donor-acceptor distance in which transfer efficiency is 0.5. FRET efficiency describes the portion of donor excitation energy that is transferred to the acceptor, which would otherwise be released in the form of light emission. As seen from the visualization of equation 4.1 in Figure 4.2, even slight changes in the distance between donor and acceptor will result in notable changes in FRET efficiency values, especially in the range close to R_0. Sensitivity of this scale makes it possible to measure distances between fluorescence-labelled sites in one macromolecule, which affords information of the conformation of the molecule. [91] Indeed FRET measurements are widely used in characterizing protein conformation, protein-protein interactions and protein-DNA interactions both *in vitro* and *in vivo*. [92–95]

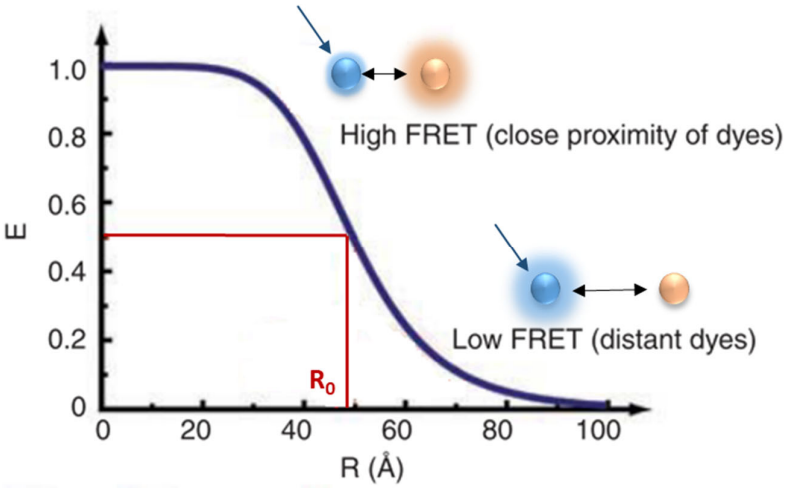

Figure 4.2: The correlation of FRET efficiency with the distance between the fluorophore dyes. Close proximity of donor and acceptor results in high FRET efficiency. Adapted from [96]

4.1 Using FRET to probe dynamic DNA origami function

The applications for FRET are not limited only to distance measurements: changes in FRET efficiency can be also monitored to follow a dynamic procedure such as hybridization of two fluorescence-labelled DNA molecules. In these applications there is no requirement for accurate definition of actual distance between the fluorophores, when the mere observation of permanent FRET increase offers enough proof of association of the two DNA molecules. [91] Hybridization can also be followed in single DNA molecules to gain information on the folding dynamics of structures of interest, such as HIV trans-activation response hairpin [97] or a G-quadruplex structure [98]. Examples from early DNA nanotechnology can also be found, such as the FRET analysis of the structure of the four-way junction [99] and characterization of the function of a nanomechanical device based on the B-Z transition of DNA [81].

This FRET analysis strategy can naturally be extended to the level of considerably larger DNA constructs, such as DNA origami. Origami structures are folded with fluorophore-functionalized staples positioned in such a way that conformational changes in the structure induce changes in FRET efficiency. Since FRET can only occur in sufficiently small distance between the donor and acceptor, assumptions of the conformation of the origami structure can be made. In the article by Andersen *et al*. [54], the function of a DNA origami box with a lid was followed utilizing this principle. The lid and the core of the box were functionalized with a donor and an acceptor, and fluorescence of the system was measured. When the box was closed FRET could be observed, but the addition of opening keys resulted in a significant drop in the efficiency thus suggesting the lid was open. The same scheme is used in many other studies which also include recyclable mechanisms [47, 88, 89, 100] and can allow even detectable delivery to a living cell [101]. Information of increasingly complex systems with more than two possible conformation states can be obtained using several fluorophores and quenchers [85].

Overall, using FRET to probe DNA origami is relatively straightforward because of the spatially predictable and controllable structure formation. Attaching fluorophores covalently to DNA is simple enough [12] and the resulting modified oligonucleotide can be added to the selected position in the origami structure as a replacement for a staple strand. Furthermore, fluorophore-functionalized staples and FRET analysis allow the observation of the origami dynamics in arbitrary conditions *in situ*, whereas

many other widely used methods (such as gel electrophoresis, AFM and TEM) require specific conditions that might interfere with the structure dynamics [102]. Although in the scope of this thesis the focus was on using FRET to gain information of origami dynamics, it is worthwhile to mention that combining FRET and DNA origami also yields other interesting applications. Examples of such are sensors [103, 104], intercellular sensors [105, 106], nanorulers [107–111] and the mapping of DNA origami folding behavior [112].

4.2 Quantification of FRET efficiency

Quantifying FRET efficiency of a donor-acceptor system enables the calculation of the distance between the fluorophores based on equation 4.1, provided that R_0 is calculated or known. However, determining the exact distance is not essential in the context of the measurements conducted in this thesis, thus this part will focus solely on the FRET efficiency calculations from the fluorescence emission data. Multiple strategies exist depending on the measurement setup and chosen donor-acceptor pair. Methods based on donor fluorescence emission intensity or lifetime change are always applicable, whereas approaches involving acceptor emission cannot be used in systems which include a quencher as the acceptor. Efficiency determination methods can also be divided into steady-state and time-resolved methods.

The steady-state method for determining FRET efficiency from donor fluorescence includes inspecting the decrease of emission intensity in the presence of the acceptor. Transfer of energy occurs as a decrease in the quantum yield (Φ) of the donor [113], which is the ratio of photons emitted to photons absorbed. Comparing the quantum yield of donor in the presence (Φ_{DA}) and absence (Φ_D) of the acceptor gives FRET efficiency *E* as:

$$E = 1 - \frac{\Phi_{DA}}{\Phi_D} \tag{4.2}$$

The relative quantum yields can be determined by measuring absorbance and fluorescence of the DA (donor and acceptor) and D (only donor) samples, assuming

that the acceptor does not emit at the donor emission wavelength. Now equation 4.2 can be written [113] as:

$$E = 1 - \frac{A_D}{A_{DA}} \frac{I_{DA}}{I_D} \tag{4.3}$$

where A_{DA} and A_D are the absorbances of the donor at the donor excitation wavelength and I_{DA} and I_D the emission intensities at the donor emission wavelength in the presence and absence of the acceptor, respectively. If donor concentration is identical in both samples and $A_{DA} = A_D$, transfer efficiency can be quantified solely based on the donor emission intensity values [91, 114], with simplified equation 4.3:

$$E = 1 - \frac{I_{DA}}{I_D} \tag{4.4}$$

Same sample scheme can be used for the lifetime-based measurements [91, 114]:

$$E = 1 - \frac{\tau_{DA}}{\tau_D} \tag{4.5}$$

where τ_{DA} and τ_D stand for the sample emission lifetimes. Lifetime-based measurements are not sensitive to concentration differences between the donor only and donor with acceptor samples, which on the other hand have a significant effect on intensity-based measurements. However, decay time method becomes increasingly complex if the donor decay is not a single exponential [91].

Using acceptor emission to quantify FRET efficiency provides an appealing alternative to donor-intensity based methods. Naturally, these methods require for the acceptor to be fluorescent as well. Calculation is carried out as follows:

$$E = \frac{\varepsilon_A(\lambda_D^{ex})}{\varepsilon_D(\lambda_D^{ex})} \left[\frac{I_{AD}(\lambda_A^{em})}{I_A(\lambda_A^{em})} - 1 \right] \left(\frac{1}{f_D} \right) \tag{4.6}$$

where $\varepsilon_A(\lambda_D^{ex})$ is the acceptor and $\varepsilon_D(\lambda_D^{ex})$ the donor extinction coefficient at the donor excitation wavelength, and can only be used in single D-A pair systems: in systems with multiple acceptors, absorbance values are used instead. f_D represents the

fractional labeling of the donor: in systems where all samples are functionalized with both donor and acceptor, $f_D = 1$. Factors $I_{AD}(\lambda_A^{em})$ and $I_A(\lambda_A^{em})$ denote the emission intensities in the presence and absence of donor at the acceptor emission wavelength. [91]

As already mentioned, reference samples without the donor or acceptor are required in each method presented. This can turn out problematic since concentrations in the intensity-compared samples should be the same, which is in practice quite difficult if not impossible. Other essential factor is the donor emission leakage to the acceptor emission spectrum (Figure 4.3), which is not accounted for in these calculations. If left uncorrected it will result in higher measured acceptor emission intensity and overestimation of FRET efficiency value.

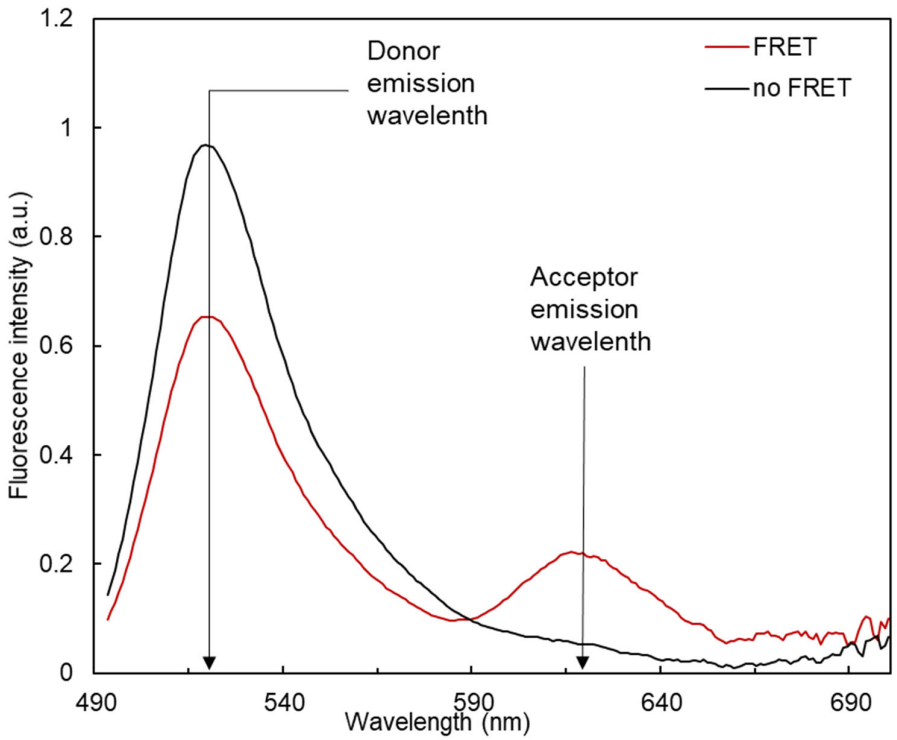

Figure 4.3: The effect of FRET on the emission spectrum of the sample after donor excitation. Donor emission intensity decreases and an increase is observed at the acceptor emission wavelength. It is noteworthy that the 'tail' of donor emission extends to the acceptor emission wavelength, hence the need for acceptor emission intensity value corrections.

The selection of a suitable method for FRET efficiency quantification is done based on the application. Occasionally a more straightforward method is desired, such as the widely used “relative” FRET efficiency E_{rel}. It is also referred to as ratiometric FRET and the proximity ratio. Relative FRET efficiency is quantified as the ratio of acceptor intensity to the total intensity:

$$E_{rel} = \frac{I_A}{I_A + I_D} \tag{4.7}$$

where I_A and I_D are the acceptor and donor intensities upon donor excitation. [115] Also here the correction of acceptor intensity value for donor emission leakage has to be taken into account. E_{rel} is not an accurate value but rather provides a satisfactory approximation of FRET efficiency. It can quite well be exploited in measurements which merely follow the changes in a dynamic system rather than determine accurate distances between fluorophores.

5 Materials and methods

The DNA origami nanocapsule analyzed in this thesis (Figure 5.1) was designed on a honeycomb lattice and has outside dimensions of ca. 31 x 28 x 33 nm. Inside of the capsule there is a cavity with dimensions ca. 11 x 12 x 13 nm that has a strand for attaching cargo such as enzymes or nanoparticles. The capsule halves are linked together from one long edge by four ssDNA 'hinges'. Halves are also functionalized with eight pairs of triplex-forming strands; ssDNA strands on the bottom and hairpin duplexes on the upper half. They will form triplexes as discussed in Chapter 2.2 that close the capsule in low pH, and the sequences are designed such that the pK_a of the capsule is estimated to be 7.2. The closed and open control capsules were prepared by replacing these with complementary strands that shut the capsule permanently or taking them out altogether. A fluorophore-functionalized staple was incorporated into each capsule halve, Alexa Fluor 488 on the top and Alexa Fluor 594 on the bottom. Capsule was also designed with poly-T overhangs in the helix blunt-end faces of the capsule to reduce aggregation (discussed in Chapter 3.1). [116]

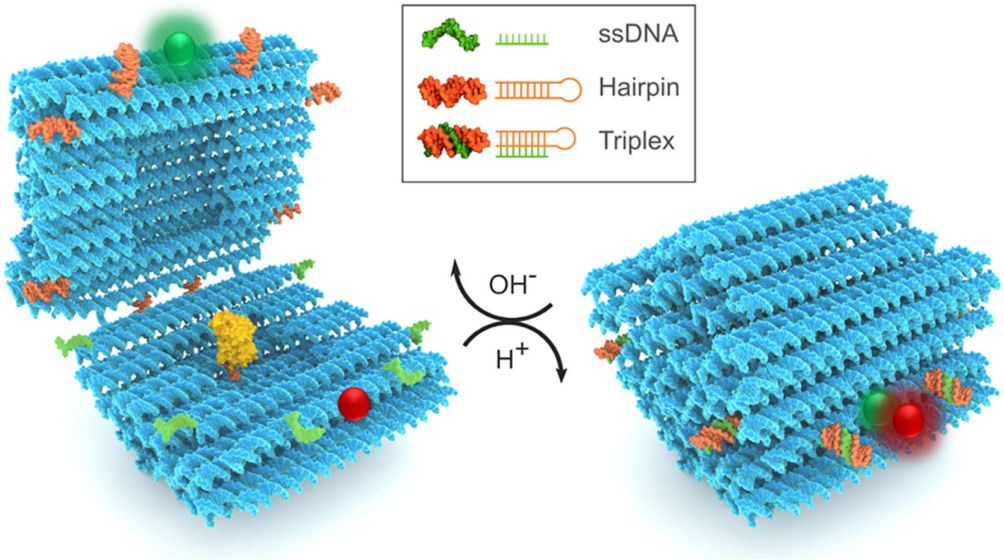

Figure 5.1: DNA origami nanocapsule. The pH-latches consist of a ssDNA strand (orange) and a DNA hairpin (green), that form a triplex when environment pH decreases (closed capsule on the right). Open capsule on the left shows the cavity inside the capsule, where enzyme cargo (yellow) has been loaded. Fluorophores are Alexa Fluor 488 (green) and Alexa Fluor 594 (red). [116]

5.1 DNA origami capsule folding and purification

The DNA origami nanocapsule was folded from single-stranded 8064 nucleotide-long scaffold (purchased from Tilibit) with 264 staples (ordered from Integrated DNA Technologies, IDT, full list available in [116]). Annealing was carried out in capsule folding buffer containing 1× TAE (tris(hydroxymethyl)aminomethane, acetic acid and ethylenediaminetetraacetic acid (EDTA)), 15 mM magnesium chloride ($MgCl_2$) and 5mM sodium chloride (NaCl). Scaffold concentration was 20 nM and staples were used in 7.5× excess.

Final folding reaction volume of 100 µl in a PCR tube was inserted into a G-storm G1 Thermal Cycler and structures were annealed with a protocol heating up to 65 ºC and then first ramping 1 ºC per 15 minutes to 59 ºC and then slowly 0.25 ºC per 45 minutes to 12 ºC. Samples were held in 12 ºC until program was manually stopped and samples then moved to 4 ºC fridge storage.

Folded structures where purified with PEG precipitation protocol adapted from [76]. Samples were first diluted in 1:4 relation with 1× capsule FOB. This solution was further diluted in 1:2 relation with PEG precipitation buffer (15% PEG 8000, 505 mM NaCl, 1× TAE). Solution was thoroughly mixed by pipetting and centrifuged in Eppendorf Centrifuge 5424 R with 14 000 g for 30 minutes. After carefully removing the supernatant the remaining transparent pellet was resuspended into 1× capsule FOB and incubated overnight in room temperature. Pellet resuspension can be performed into 1× capsule FOB with modified pH for the measurements that require samples in different conditions.

5.2 DNA origami capsule analysis

Absorbance of purified DNA origami samples were determined with UV/VIS spectroscopy using BioTek Eon Microplate Spectrophotometer or BioTek Cytation3 Multi-Mode reader and Take 3 Microvolume Plate. Absorbances measured in DNA maximum absorption wavelength 260 nm were used to estimate the DNA origami capsule concentration using the Beer-Lambert relation:

$$A_{260} = \varepsilon_{260} c_{orig} l, \tag{5.1}$$

where A_{260} is the absorbance at 260 nm (DNA absorbance maximum [12]), ε_{260} is the estimated extinction coefficient for the DNA origami nanocapsule at wavelength 260 nm (1.047×10^8 $M^{-1}cm^{-1}$ [116]), c_{orig} is the concentration of origami and *l* the length of the light path (0.05 cm). Theoretical maximum value for the capsule concentration is the same as the scaffold concentration (20 nM).

The folding quality of DNA origami nanocapsule structures was investigated with an electrophoretic mobility shift assay (EMSA). 2 w-% agarose gels were prepared with 1× TAE and 11 mM $MgCl_2$, and dyed with ethidium bromide (EtBr). Scaffold p8064 diluted with 1× FOB was used as a reference (1.5 µl scaffold, 8.5 µl 1× capsule FOB). 10 µl samples were loaded with 2 µl of 6X loading dye (New England Biolabs). Gels were run with 90 V for 50 minutes on an ice bath using BIO-RAD Power Pac Basic equipment and imaged with BioRad ChemiDoc XRS+ or BioRad ChemiDoc MP imaging system.

BioRad ChemiDoc MP imaging system includes also fluorescence channels for gel imaging. The system contained defined channels for Alexa Fluor 488 (excitation filter 470/30 and emission filter 532/28) and Alexa Fluor 546 (excitation filter 530/28 and emission filter 602/50) detection, which were used in the capsule characterization in varying EMSA conditions. In addition to the above described TAE buffer system with pH 8.2, a more acidic combination with pH 6.4 was used. It contained 45 mM MES (2-(*N*-morpholino)ethanesulfonic acid) and 25 mM tris (tris(hydroxymethyl) aminomethane) with 11 mM $MgCl_2$, and the pH of the solution was adjusted with 10 M NaOH (sodium hydroxide). Gels were prepared without EtBr to avoid interfering emission at Alexa 546 channel, and loaded with self-prepared loading dye mixture (1× loading dye contains 2.5 w-% Ficoll 400, 3.3 mM Tris-HCl, 0.015 w-% bromophenol blue).

5.3 Fluorescence measurements

Fluorescence measurements were conducted with BioTek Cytation 3 Multi-Mode reader using Costar black flat bottom 96-well plates. Emission spectra were recorded using excitation wavelength of 460 nm for the donor and 560 nm for the acceptor. Read height was set to 7 mm, and 15 measurements per data point were taken. In kinetic measurements samples were excited at 460 nm, and emission was recorded

at 517 nm for donor and 616 nm for acceptor. In some measurements also acceptor emission from direct excitation was quantified (excitation at 560 nm, emission measured at 616 nm). Data points were 30 seconds apart with 30 measurements per data point and 7 mm read height. The sample pH was cycled by adding 2-4 µl portions of 0.5 M acetic acid (AcAc) or sodium hydroxide (NaOH) with a multichannel pipette and mixing samples.

5.4 FRET efficiency calculation

Extinction coefficient values for the fluorophores at the 460 nm and 560 nm excitation wavelengths were defined using the values provided by IDT for the absorbance maxima (Table 5.1) and measured absorbance spectra of the used fluorophore-modified oligonucleotides. Absorbance spectra were measured form 10 µM solutions of the individual oligonucleotides, and the values from excitation wavelengths 460 nm and 560 nm in relation to the measured maxima were used to determine the extinction coefficients. Calculations yielded 30 817 $M^{-1}cm^{-1}$ for the acceptor at acceptor excitation wavelength (ε_{AA}) and 19 848 $M^{-1}cm^{-1}$ and 1 985 $M^{-1}cm^{-1}$ for the donor and acceptor at donor excitation wavelength (ε_{DD} and ε_{AD}).

Table 5.1: Absorption and emission properties of the used fluorophore-modified oligonucleotides. IDT values acquired from [117]

	Absorption max.		**Emission max.**		**Extinction coefficient at abs.max. (IDT)**
	Measured	**IDT**	**Measured**	**IDT**	
Alexa 488	493 nm	492 nm	518 nm	517 nm	65 000 $M^{-1}cm^{-1}$
Alexa 594	594 nm	584 nm	616 nm	616 nm	80 000 $M^{-1}cm^{-1}$

Emission spectra of all samples was smoothed using moving average with factor 4. This was done prior to FRET efficiency calculations to avoid using falsely extreme intensity values caused by the fluctuation of the emission signal. The acceptor emission intensity values also had to be corrected for donor emission leakage, as discussed in Chapter 4.2. This was done by folding a capsule sample with only the donor fluorophore and recording both full emission spectrum and kinetic emission intensity values after donor excitation. Correction factors were calculated from these

emission intensities, and they were 0.0077 for kinetic and 0.0363 for spectral data. Then, using them in equation 5.2 yielded the corrected acceptor emission values:

$$I_{AD} = I_{AD} - CF * I_{DD} \tag{5.2}$$

where I_{AA} is the acceptor and I_{DD} the donor emission intensity following donor excitation, and *CF* the correction factor for either spectral or kinetic data.

The quantification of FRET efficiency was decided to be done by determining the acceptor emission increase upon donor excitation, and using the same sample as an internal reference for the acceptor emission without energy transfer by exciting it on a wavelength where the donor does not absorb (560 nm). This was considered as the best strategy, since it is quite difficult to ensure exact same concentrations between two DNA origami samples. The final formula used for the quantification of the energy transfer efficiency was derived starting from the definition of quantum yield, which is the proportion of photons emitted to photons absorbed:

$$\phi_A = \frac{I_A(\lambda_{ex})}{A_A(\lambda_{ex})} \tag{5.3}$$

$$I_A(\lambda_{ex}) = \phi_A A_A(\lambda_{ex}) \tag{5.4}$$

where ϕ_A is the quantum yield of the acceptor, $I_A(\lambda_{ex})$ is the emission intensity of the acceptor after excitation at determined wavelength and $A_A(\lambda_{ex})$ is the absorption of the acceptor in that excitation wavelength. In this case the acceptor emission is measured following two different excitation wavelengths: emission intensity I_{AD} at the excitation wavelength of the donor and I_{AA} at the excitation wavelength of the acceptor. These values have to be compared to the corresponding absorbance values, which are acceptor absorbance at the donor excitation wavelength (A_{AD}) and acceptor absorbance at the acceptor excitation wavelength (A_{AA}). For the acceptor emission intensity following donor excitation:

$$I_{AD} = \phi_A A_{AD} \tag{5.5}$$

This is true as long as the emission intensities are a product of direct acceptor excitation at said wavelength only. In case there is energy transfer from a donor, the

emission intensity I_{AD} consists of the result of direct excitation ($I_{AD}(direct)$, equation 5.YY) and the emission that results from FRET ($I_{AD}(FRET)$). It is a result from donor absorption at donor excitation wavelength (A_{DD}), the efficiency of FRET (*E*) and the quantum yield of the acceptor:

$$I_{AD}(FRET) = \phi_A A_{DD} E \tag{5.6}$$

Combining acceptor emission intensities from direct excitation (equation 5.5) and from FRET (5.6) yields:

$$I_{AD} = I_{AD}(direct) + I_{AD}(FRET) = \phi_A A_{AD} + \phi_A A_{DD} E$$

Here ϕ_A can be written as the relation between I_{AA} and A_{AA} according to equation 5.3, because I_{AA} does not contain the energy transferred through FRET since the acceptor is excited on a wavelength where the donor does not absorb. This yields:

$$I_{AD} = \frac{I_{AA}}{A_{AA}} A_{AD} + \frac{I_{AA}}{A_{AA}} A_{DD} E$$
$$E = \frac{A_{AA}}{I_{AA} A_{DD}} \left(I_{AD} - \frac{I_{AA} A_{AD}}{A_{AA}} \right)$$
$$E = \frac{I_{AD} A_{AA} - I_{AA} A_{AD}}{I_{AA} A_{DD}}$$

Since the used fluorophores are embedded into the DNA origami structure as functionalized staple strands, it is quite safe to assume that donor and acceptor are present in 1:1 relation. Thus extinction coefficients can be used instead of absorbances (based on equation 5.1). This yields:

$$E = \frac{I_{AD} \varepsilon_{AA} - I_{AA} \varepsilon_{AD}}{I_{AA} \varepsilon_{DD}} \tag{5.7}$$

This equation does not take into account the leaking of donor emission into the acceptor emission wavelength discussed in Chapter 4.2. Thus the FRET efficiency is quantified using equation 5.7 with I_{AD} values corrected by equation 5.2. The same correction (with different correction factor) was done for acceptor emission intensities in kinetic measurements. However, there the efficiency of energy transfer was

estimated by the ratiometric FRET method (equation 4.6). This is largely because the single wavelength detection in kinetic measurements yielded donor and acceptor emission intensity values with a different relation than in the spectral measurements.

6 Results and discussion

This chapter presents the most important results obtained with the methods introduced in Chapter 5. They include the analysis of the folding of the DNA origami nanocapsules, FRET analysis of the capsule conformation and the changing kinetics, the effects of salt concentrations in the capsule function and the investigation of the correlation between FRET efficiency and environment pH. Also some fluorescence characterized EMSA of the capsules is presented. The significance of the results is also discussed as they are presented.

6.1 Analysis of the folding of origami capsules

The folding of DNA origami nanocapsules and the success of the PEG purification were assessed with electrophoretic mobility shift assay as described in 5.2. In the EMSA, pH-latch capsules were compared to open and closed control capsules, and from each capsule type two PEG purified samples (resuspended to 1× capsule FOBs, pH 6.2 and pH 8.2) were included in addition to the unpurified sample. From the EMSA result in Figure 6.1, it can first be noted that PEG purification of capsules is successful: the band with the excess staples is greatly diminished in the purified samples (B and C) compared to the unpurified ones (A). Excess staple strands are much smaller than any of the folded/misfolded structures, which means that they migrate the furthest.

The mobility of the purified origami samples in pH 8.2 1× capsule FOB were compared with the scaffold reference, which was in the same buffer. Slightly further migration was observed in the purified origami samples, which indicates that they are folded. Correct structure was further verified with TEM (Figure 6.2 and Appendix A Figures A1 and A2). At least two bands were visible for each sample, which suggests that there are multiple superstructures present. It is probable that the leading band with greatest mobility contains the capsule monomers, whereas the lagging band(s) represent capsule aggregates in varying sizes, such as capsule dimers.

It was hypothesized that the conformation of the capsule should be shown in the mobility difference; open capsules would be slower since closed capsules are folded into a more compact structure that should be able to go through the agarose faster. For this reason, purified samples resuspended into pH 6.2 1× capsule FOB were also

prepared from each capsule type (samples C in Figure 6.1). The lower pH samples were needed because the pH-latch capsules should be closed at pH 6.2, and the hypothesis was that a change in electrophoretic mobility would be observed between the pH-latch samples at different pHs, which could indicate a shift in the capsule conformation. However, it seems that the change in mobility is sample pH- dependent rather than direct result of the assumed capsule conformation differences, since even the open control at pH 6.2 migrates faster than the same sample resuspended into pH 8.2. It was also considered that even though the samples were pipetted onto the gel wells at pH 6.2 they were unlikely to remain that way, since the running buffer pH in TAE gels was 8.2. Thus more acidic running buffers would be needed for the pH-latch capsules to be able to remain closed during the EMSA experiment. This was investigated in Chapter 6.6.

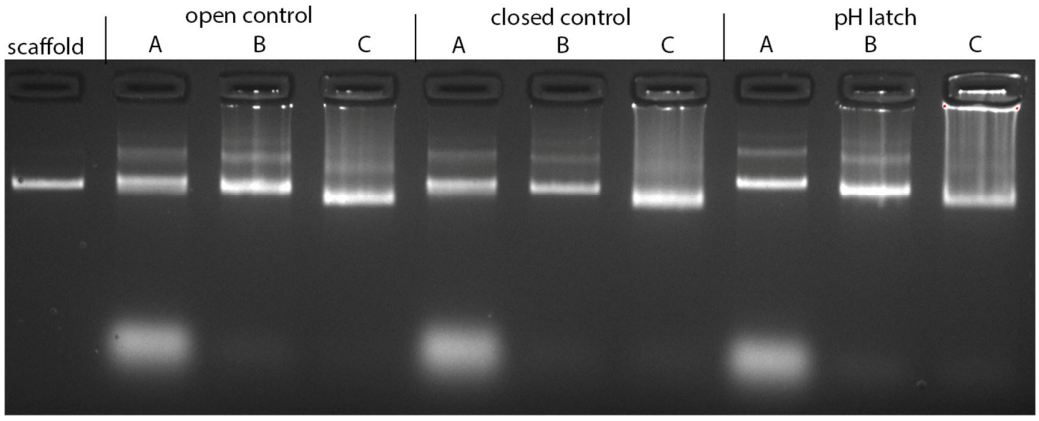

Figure 6.1: Analysis of DNA origami nanocapsule folding with EMSA. First line contains the p8064 scaffold reference. Following lanes have A, B and C samples from open control, closed control and pH-latch capsules. A = unpurified, B = PEG purified to pH 8.2, C = PEG purified to pH 6.2.

6.2 FRET analysis of the capsule conformation

The capability of the DNA origami nanocapsule to adopt both the closed and open conformations was investigated with spectral FRET measurements. Capsule samples were prepared at two different pH-solutions (pH 8.0 and pH 6.4), and the fluorescence spectra were measured with 460 nm excitation (donor excitation wavelength). In addition, open and closed control samples were prepared and analyzed in these same

conditions. Observing the pH-latch sample spectra shows that a peak for acceptor emission emerges at the lower pH (Figure 6.2 b), which suggests that the majority of the capsules are in closed conformation. The shape of the spectrum is also well in line with the closed control, whereas at pH 8, the shape of pH-latch sample spectrum resembles the open control (Figure 6.2 a). Importantly it is also observed that the spectra of the controls remain the same regardless of the sample pH, which further confirms that the observed change in fluorescence is due to energy transfer in the sample and not environmental conditions.

Spectra with 560 nm excitation was also recorded from all samples to calculate values for FRET efficiency according to equation 5.7. FRET efficiency for open control at both pHs remains at approximately zero, whereas values for closed control are above 0.75. The efficiency values for the pH-latch sample are approximately zero at pH 8.0 and rise as high as 0.90 at pH 6.4. The variation in efficiency values is another way to describe the shift observed in the emission profile of the pH-latch sample, which both indicate a significant change in the conformation of the capsules bringing the fluorophores closer together. This is further supported by TEM images taken from pH-latch samples at corresponding pHs (Figure 6.2 and Appendix A, Figure A2) and comparing them to TEM pictures taken from the control samples (Appendix A, Figure A1). Capsules in pH-latch sample at pH 8 have their halves in varying distances from each other, which indicates that they have been free to fluctuate in the scope given by the hinges. When sample pH is decreased, the pH-latch capsules appear to be for the most part in closed conformation that closely resemble the TEM imaged structure of the closed control capsules.

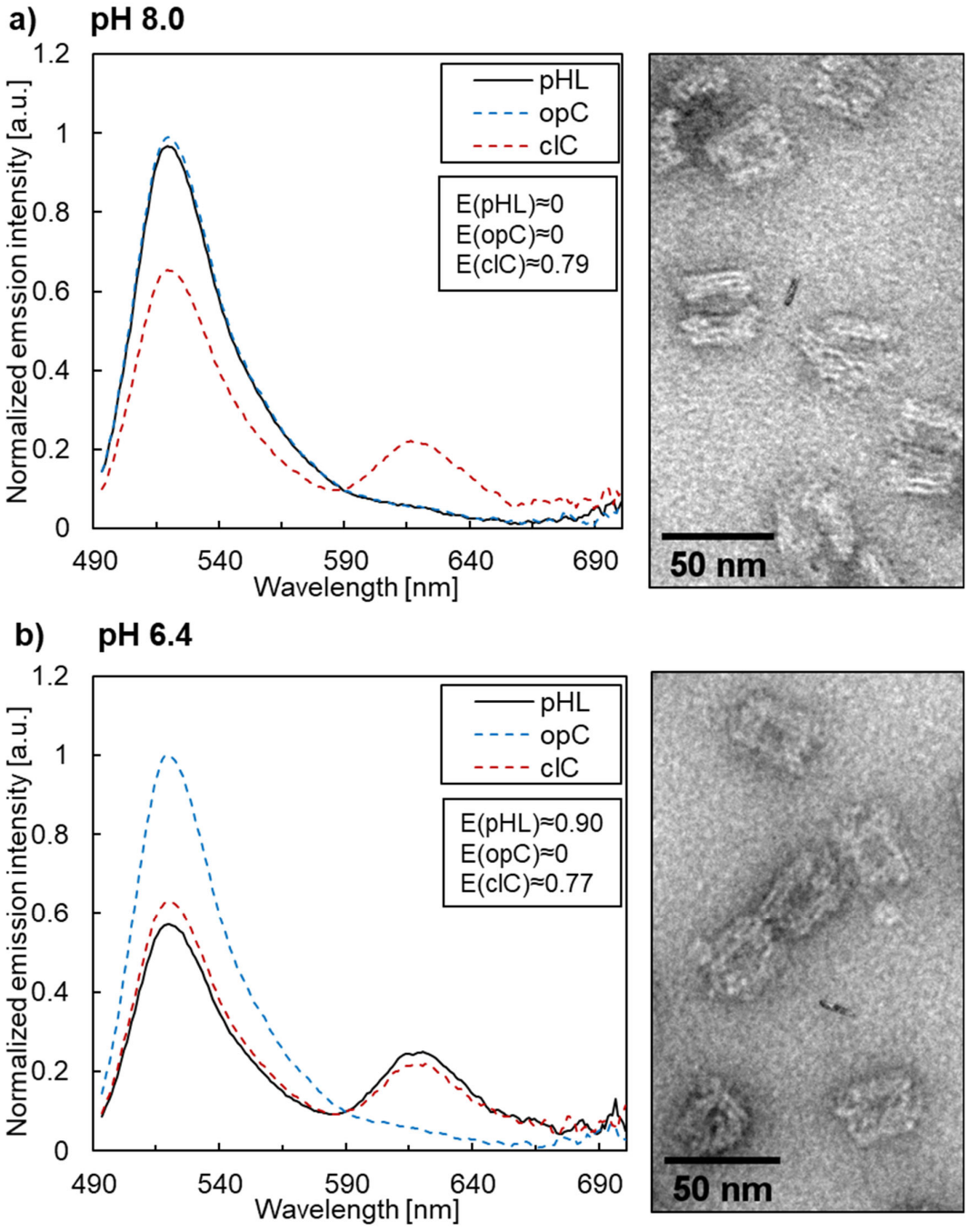

Figure 6.2: Emission spectra of pH-latch capsules (pHL) with open and closed controls (opC and clC). Insets show the FRET efficiency values calculated form the spectral data and TEM images taken from the pH-latch sample. a) All samples resuspended into pH 8.0, b) all samples in pH 6.4. TEM images adapted from [116].

The FRET efficiency value of 0.90 should in principle show as 90 % decrease in the emission intensity of the donor, yet this is not observed in the pH-latch sample spectrum at pH 6.4 (Figure 6.2 b). Thus there is likely some error in the FRET efficiency quantification. One possible source of error can be inaccuracies in the extinction coefficient determinations (Chapter 5.4). In the calculation, values provided by IDT were combined with experimentally determined absorbance maxima, and the measured wavelength for acceptor absorption maximum was off as much as 10 nm from the IDT provided one (Table 5.1). Apart from the calculations, there might be some unexpected interactions in the system that are causing the inconsistencies observed between the donor emission decrease and calculated FRET efficiency values. However, the values calculated are sufficient for this thesis, as the goal is not the exact quantification of the distance between the fluorophores but bringing together proof of conformational changes in the capsule system. Moreover, the assumptions of the conformation of the capsules made based on the calculated efficiency values are verified with TEM, which provides assurance of their validity.

6.3 FRET analysis of capsule kinetics

The capability of the capsules to shift between open and closed conformations and the kinetics of the process were studied with kinetic fluorescence measurements. Measurement was started with capsules at pH 8.0, from which the pH was lowered to 6.2 and the changes in the pH-latch sample fluorescence signal were compared to the open and closed controls (Figure 6.3). After closing, sample pH was again increased to 8.0 to open the capsules. Changes in efficiency of the energy transfer were followed by calculating relative FRET efficiency. The spectra shows that there is a clear change in the FRET efficiency of the pH-latch sample. In starting pH 8.0, it is at the same level with the open control, but after environment pH decreases, the relative FRET efficiency starts to increase as well. It can be quite safely stated that when the relative FRET efficiency values reach those of the closed control, majority of the capsules are closed. When sample pH is increased again, pH-latch sample FRET efficiency returns to the level of the open control.

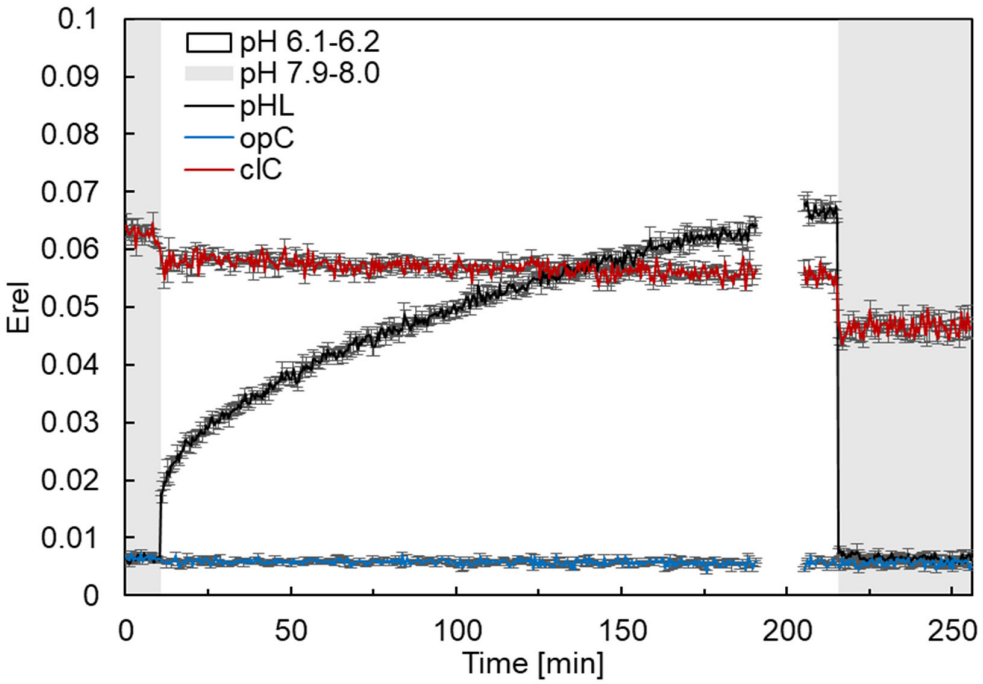

	pH 8.0	pH 6.2	pH 8.0
	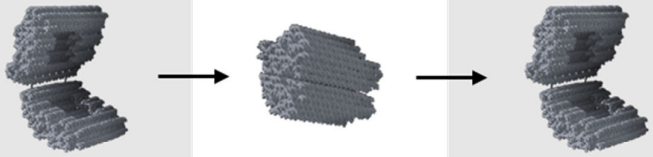		
pH latch	-0.008 ± 0.020	0.67 ± 0.02	-0.035 ± 0.006
Open control	0.020 ± 0.006	-0.006 ± 0.008	-0.06 ± 0.02
Closed control	0.66 ± 0.02	0.600 ± 0.003	0.43 ± 0.01

Figure 6.3: Kinetic measurement of the dynamics of pH-latch capsules (pHL) with open and closed controls (opC and clC). Error bars represent the standard error of the mean of three parallel samples. Bottom panel shows FRET efficiency value as the mean calculated from the full emission spectra of the three parallel samples measured within the kinetic experiment, with standard error of the mean. The schematic capsule represents the presumed conformation of the pH-latch capsules.

It is noteworthy that the timescale in which the opening and closing conformational shifts occur are quite different. Opening of the capsule is very rapid: relative FRET

efficiency has returned to the open control level even before the first measurement point is taken after the pH change, which is at 30 seconds. The closing on the other hand takes much longer, as the FRET efficiency of the pH-latch sample reaches the level of the closed control after approximately 125 minutes. This is to be expected since the closing is a multi-step process: first the fluctuating capsule halves have to reach a closed (or nearly closed) conformation, after which the pH-latch triple-helices have to associate. The folding of negatively charged DNA structure to an even tighter conformation is not energetically favorable, thus it is speculated that positive ions in the solution are essential for the closing mechanism to work. The logical result is that the opening of the capsule is a rapid process, since it only requires the disassembly of the pH-latches after which the capsule halves are free to spring out in a more energetically favored conformation.

The use of relative FRET efficiency to follow the capsule kinetics is justified since the interest is to observe changes within the pH-latch sample in relation to open and closed controls. However, also full emission spectra were measured before each acid or base addition to verify the conformation of the capsule in that time point. FRET efficiency values were calculated from the full emission spectra, and are compared in Figure 6.3. It is also noteworthy that the relative FRET efficiency and FRET efficiency values are not in the same scale (discussed in Chapter 5.4).

The next appealing step was to test whether the closing and opening cycle could be repeated multiple times. For this, five consecutive close-open –cycles were executed (Figure 6.4). In this experiment a shorter stabilization time of 90 minutes in acidic pH was used. Nevertheless it appears that the capsule closes, which was verified from the profiles of the full emission spectra measured before each environment pH change. Five consecutive cycles were successfully performed. Interestingly, a drop in the relative FRET efficiency value of the closed control was observed following each NaOH addition, which did not affect the other samples in the same way.

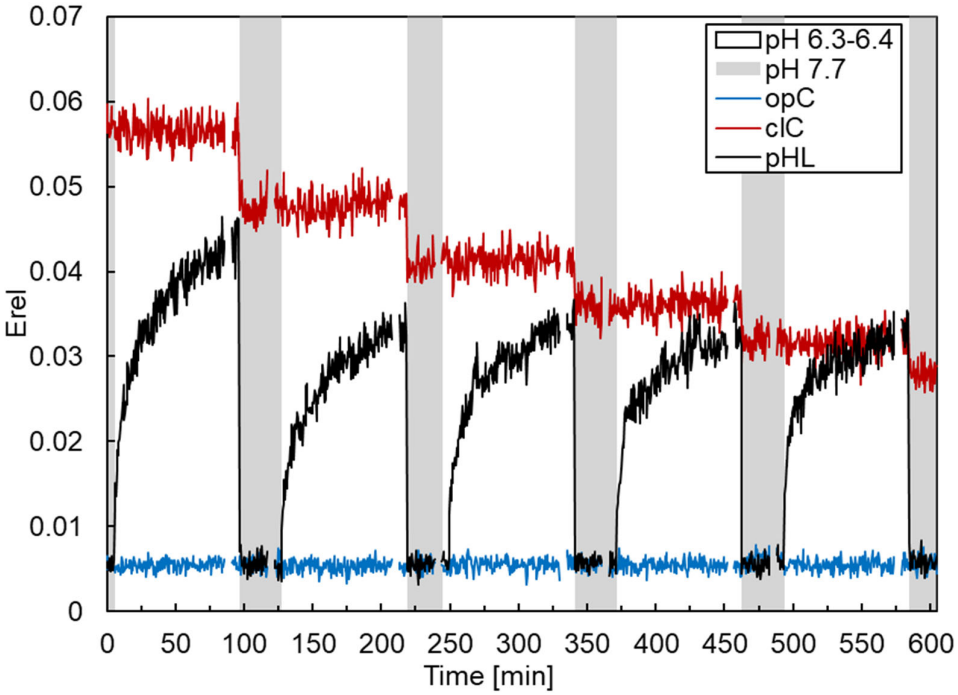

Figure 6.4: Five-cycle measurement of a pH-latch sample (pHL) with open and closed controls (opC and clC).

Samples for TEM imaging were also taken after the first and fifth closing to investigate the details of the possible effect of the consecutive cycles on the capsule structure. The samples taken from the closed control (Figure 6.5 and Appendix A, Figure A3) were especially interesting in the light of the decreasing relative FRET efficiency observed in the kinetic measurement (Figure 6.4). TEM images show that the amount of deformed capsule structures is greater in the sample taken from the fifth cycle. As the drop in relative FRET efficiency was observed in response to each NaOH addition, the first concern was to rule out the possible effect of the increasing Na^+-ion concentration. This is further discussed in the next chapter.

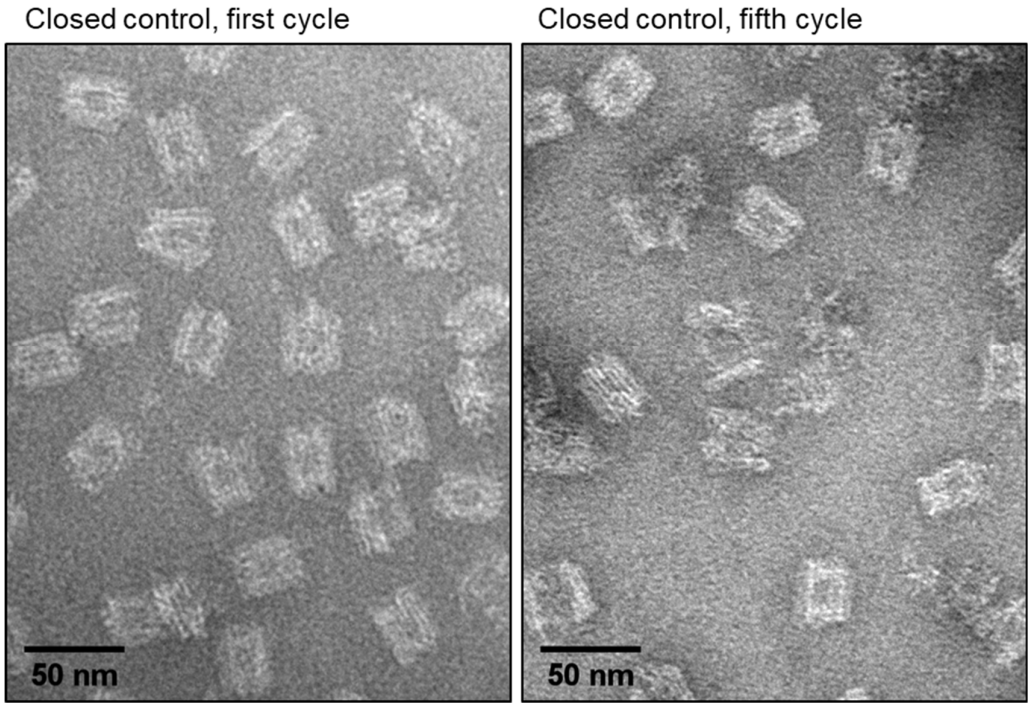

Figure 6.5: TEM images of closed control samples taken in the five-cycle experiment. Adapted from [116].

6.4 MgCl and NaCl effects

The aforementioned effect of sodium ions was tested with the same kinetic measurement setup with 4 µl additions of 0.5 M sodium chloride (NaCl) instead of sodium hydroxide. Figure 6.6 shows the result of the measurement; the stair-shaped pattern is not observed and relative FRET efficiency remains in the same level throughout the NaCl additions.

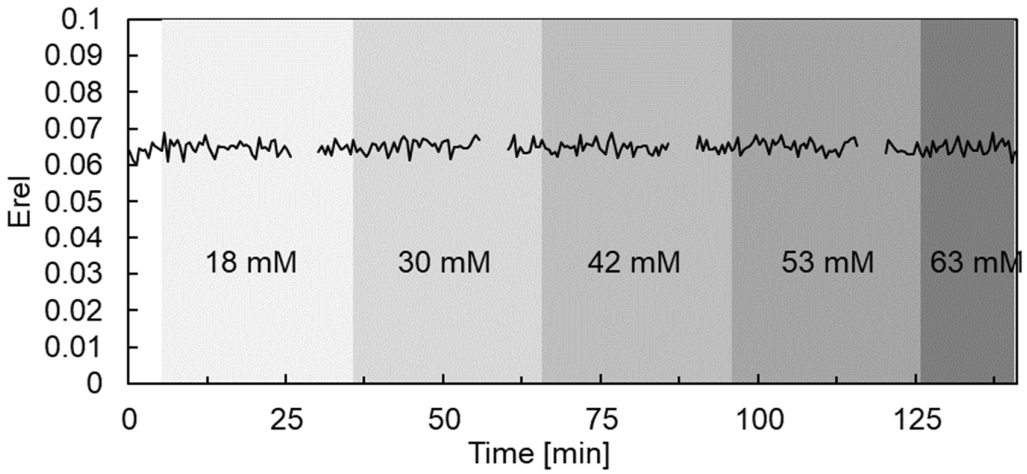

Figure 6.6: Investigating the effect of increasing NaCl concentration on the relative FRET efficiency of the closed control. The concentration increase is indicated in the figure background color with the concentration value.

Encouraged by these results the integrity of the capsule conformation was further investigated in physiological salt concentration (150 mM NaCl). This can be considered as an essential factor in the light of possible *in vivo* –applications in the future. As both kinetic (Figure 6.7 a) and spectral (Figure 6.7 b) data show, the addition of 150 mM NaCl has no effect on the capsule conformation. However, the role of divalent Mg^{2+} -ions in origami solutions is known to be more significant, which is why the effect on the capsule closing kinetics was tested. Concentrations of 15 mM, 10 mM and 5 mM were chosen, and the closing of the samples followed with relative FRET efficiency. From the resulting spectra (Figure 6.7 a) it is seen that the concentration of $MgCl_2$ significantly affects the rapidity of the closing: decrease in divalent ions in the solution slows the process down. Moreover, based on the low FRET efficiency values (Figure 6.7 c) it appears that the capsules do not close properly at 5 mM $MgCl_2$, or that the amount of closed capsules is small.

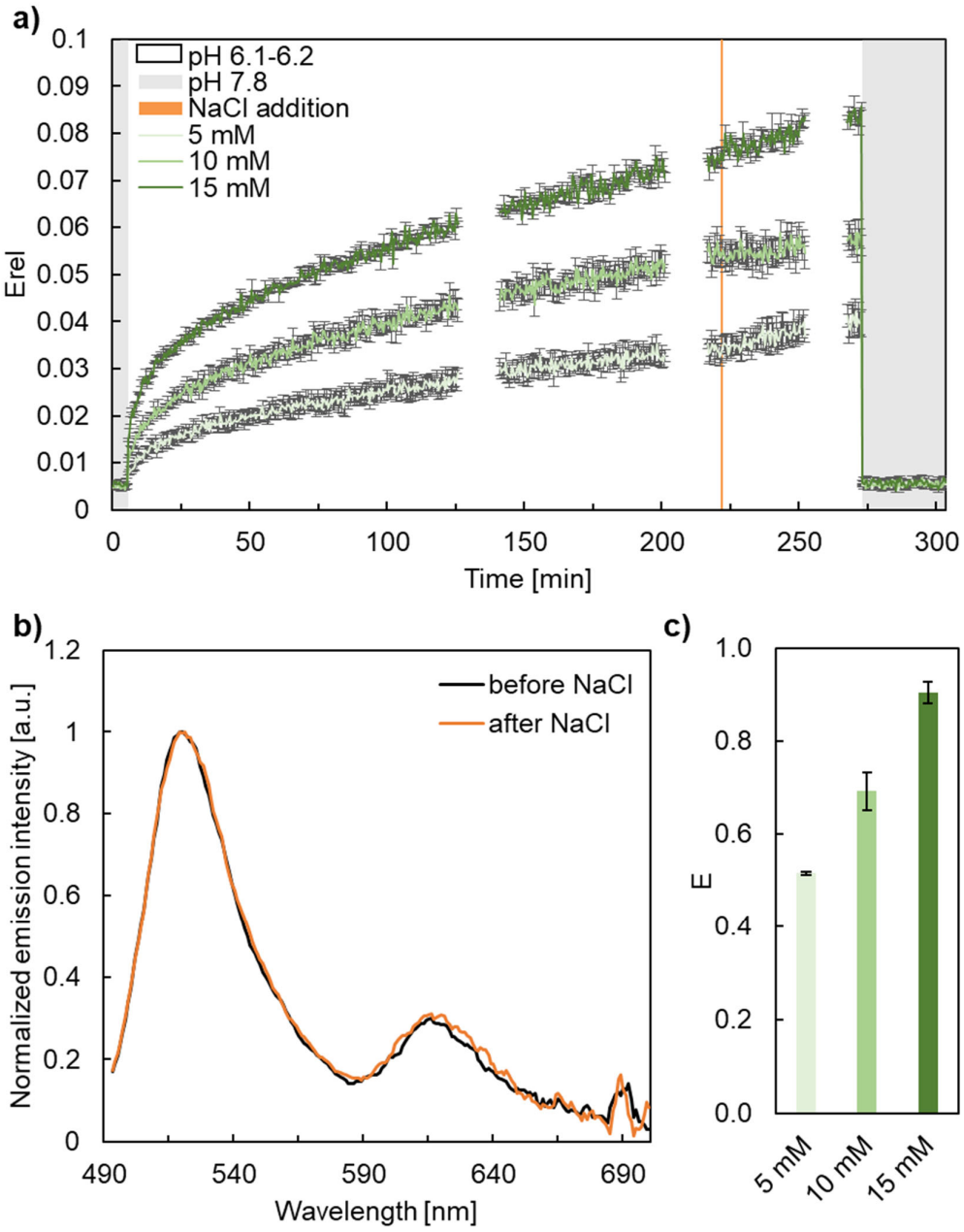

Figure 6.7: Investigating the effect of $MgCl_2$ concentrations on pH-latch samples with addition of 150 mM NaCl. a) Kinetic measurement of pH-latch samples in three $MgCl_2$ concentrations (5, 10 and 15 mM). Error bars represent the standard error of the mean from three parallel samples. b) Emission spectra (460 nm excitation) of 15 mM $MgCl_2$ pH-latch capsule sample before and after the addition of 150 mM NaCl. c) FRET efficiencies calculated from the emission spectra of samples form a) before increasing the pH. Error bars represent the standard error of the mean from three parallel samples.

These observations are in line with the speculations made in Chapter 6.3: the rapidity of the closing process is dependent on the extent of fluctuation in the capsule structure, since the halves have to be close enough for the pH-latch triplexes to form. This is greatly affected by the solution cation concentration, as counteracting the electrostatic repulsion between the negatively charged capsule halves increases the probability for them fluctuate to a conformation with sufficient proximity for the triplex formation. It is probable that the triplex is also more stable, since it benefits from the reduction of electrostatic repulsion as well. Based on the $MgCl_2$ concentration experiments conducted it can be stated that 15 mM is required for the sufficient closing of the capsule. Increasing the $MgCl_2$ further will speed the process but also result in significantly greater aggregation between the capsules.

6.5 Effect of pH on FRET efficiency

The FRET efficiency pH-responsivity was further investigated by a titration curve experiment. 11 capsule samples were diluted after PEG purification into buffers from pH range 8.0-6.0 with 0.2 pH unit intervals. The emission spectra of these samples was recorded and FRET efficiencies calculated to yield a curve that illustrates the correlation between pH-change and energy transfer efficiency (Figure 6.8). Firstly, it can be stated that the pH-latch sequence -based estimation of the system pK_a (7.2) was quite accurate, since it seems that the transition between capsule conformations occurs in pH range 6.8-7.6. Above pH 7.6 the capsule is in open conformation, and $E \approx 0$. Below 6.8 the capsule is clearly in closed conformation, and the FRET efficiency value settles around $E \approx 0.69$ at pH 6.8-6.4. However, when the pH is decreased even further, FRET efficiency value increases again rather steeply. This is speculated to be due to capsule aggregation rather than even closer proximity of the dyes within one capsule. Formation of aggregates does not seem to be as significant problem at higher pHs. Thus it can be speculated to occur due to some sort of interactions between the pH-latch strands of different capsules. This theory is supported by the observation that aggregation does not seem to be as severe problem in open or closed controls, which was noticed also in EMSA experiments (Figure 6.1), where pH-latch sample at pH 6.2 was the only one with significant aggregation.

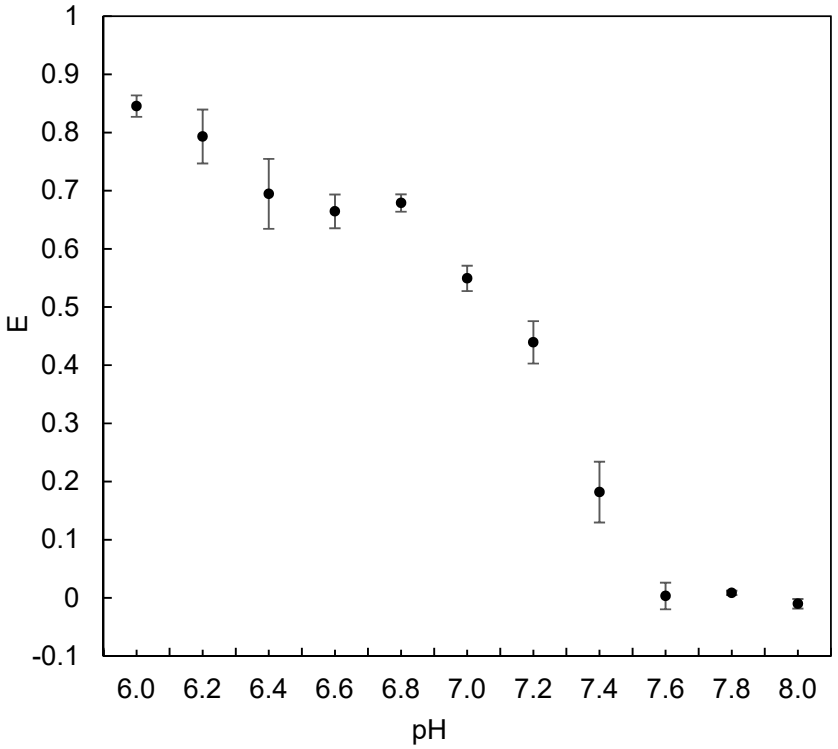

Figure 6.8 pH titration experiment. Three parallel samples from each sample pH analyzed. Error bars represent standard error of the mean.

6.6 Fluorescence characterized EMSA

The capsule samples were further investigated with EMSA at lower pH buffer system, which was thought to be essential for the pH-latch capsules to be able to remain in closed conformation (as discussed in Chapter 6.1). Moreover, the bands were visualized using fluorescence imaging filters suitable for the fluorophores in the capsules rather than visualizing DNA with EtBr. This would allow the detection of possible changes in the fluorescence of the samples in relation to their mobility in the gel. The ideal setup would have been to be able to use the same excitation and emission filters as used in the fluorescence measurements conducted with the plate reader, which would have enabled the detection of FRET in the samples. As this was not possible with the available equipment, the emission of both donor and acceptor were measured separately and then combined into the same image. Thus possible FRET could not be detected from the acceptor emission intensity increase but from decrease in the donor emission.

A gel was prepared in MES/Tris buffer with pH 6.4, and compared to the ‘normal’ TAE gel with pH 8.2 (Figure 6.9). First of all it must be stated that the channel Alexa Fluor 546 used for the detection of acceptor (Alexa Fluor 594) fluorescence was not a perfect fit, which somewhat accounts for the detected lower intensity bands compared to the ones imaged with Alexa Fluor 488 channel (the donor detection channel). Thus it is noteworthy that in the TAE gel the band for closed control appears red (Alexa Fluor 546 channel) whereas the pH-latch and open control samples have bands that are more intensely green (Alexa Fluor 488 channel). This suggests that the donor emission is not as strong in the closed control sample, which can be a result from part of the energy absorbed by the donor being transferred rather than emitted. Thus there is FRET in the sample which indicates closed conformation. Additionally the pH-latch sample resembles the open control rather than the closed control, which is as it should at pH 8.2.

The lower pH EMSA gives bands with different mobility, which is due to the use of MES/Tris buffer system rather than TAE. This was done because TAE is not capable of buffering efficiently at pHs as low as 6.4. The open control on the MES/Tris gel gives a quite similar band as in TAE gel with strong emission in the donor channel. In closed control band the signal from donor emission is fainter, and signal from acceptor emission is also clearly visible. The diminished donor emission signal would again suggest that there is FRET in the sample. Importantly in this gel the pH-latch sample resembles the closed control more than the open, since the acceptor emission signal is observed in the capsule band rather than being veiled by the donor signal. However, the entire band observed from the pH-latch sample is quite dim, which is due to a portion of the sample remaining next to the well. This indicates that there are large aggregates present in the sample, which has been recognized as a problem with the pH-latch samples at low pHs in the earlier samples as well. In this case the aggregation might be worse than predicted based on the spectral results at pH 6.4 because the pH of the running buffer had a tendency to decrease during the EMSA experiment. A proper solution to this problem was not yet found even though different combinations of the buffer components were tried: the attempt reported here produced the best outcome. Due to the aggregation problem no conclusions can be drawn from the pH-latch sample emission intensities. It is probable that the capsule system is too delicate to be reliably characterized with EMSA.

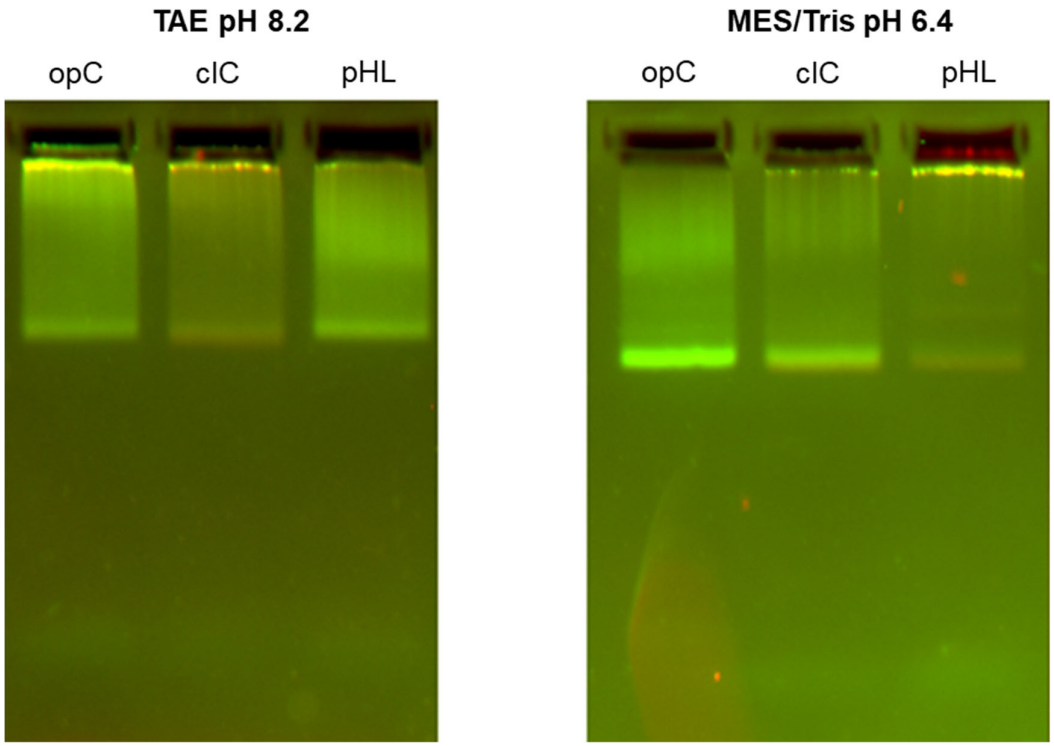

Figure 6.9: Fluorescence characterized EMSA. Filters used for imaging were Alexa Fluor 488 (green) and Alexa Fluor 546 (red). All samples were diluted in PEG purification to 1× capsule FOB at the same pH with the gel running buffer. Open and closed controls (opC and clC) were run with the pH-latch sample (pHL).

7 Conclusions

The aim of this thesis was to demonstrate the function of a dynamic DNA origami nanocapsule using Förster resonance energy transfer analysis. FRET characterization was supported with transmission electron microscopy (TEM) and electrophoretic mobility shift assay (EMSA). The results show that the capsule can effectively open and close in response to external pH changes. Kinetic studies showed that opening of the capsule is very rapid, whereas closing process requires more time and is affected by the Mg^{2+} concentration in the solution. However, closed pH-latch capsule remains intact when exposed to physiological salt concentration (150 mM NaCl). It is also shown that the closing and opening of the capsule can be performed for multiple consecutive cycles.

The characterized pH-response range of the capsule system is well in line with the values predicted based on designed pH-latch sequences and previous results from other groups [83, 84]. This suggests that it would be possible to tune the pH-response with changing the pH-latch sequence composition. The rationally designable pH-response occurring in a range of roughly 0.8 units can be exploited in a multitude of applications, such as targeting cancer cells with inverted pH gradient [118].

Next step towards the applications would be to investigate the capsule system with enzyme cargo to ensure proper function of the pH-latches. The effectivity of the encapsulation of the enzyme should be tested, as ideally the accessibility of the enzyme would be significantly restricted when inside a closed capsule, yet the enzyme ought to remain functional when the capsule is opened. Moreover, the stability of the capsule in cells should be examined. Prospective complications might arise from early degradation of the capsule structure by deoxyribonuclease I. Additionally, the capsules might provoke an unwanted immune response. These problems could be addressed by coating the capsule e.g. with a suitable protein [119, 120]. This strategy could improve the stability and protect the capsule from immune response, as well as enhance the delivery rate into cells. Naturally, capability of the coated capsule to adopt the open and closed conformations and the function of the pH-latches should be thoroughly ensured.

8 References

[1] N. C. Seeman and N. R. Kallenbach, “Design of immobile nucleic acid junctions,” *Biophys. J.*, vol. 44, pp. 201–209, 1983.

[2] P. W. K. Rothemund, “Folding DNA to create nanoscale shapes and patterns,” *Nature*, vol. 440, no. 7082, pp. 297–302, 2006.

[3] H. Ijäs, S. Nummelin, B. Shen, M. A. Kostiainen, and V. Linko, “Dynamic DNA origami devices: From strand-displacement reactions to external-stimuli responsive systems,” *Int. J. Mol. Sci.*, vol. 19, no. 7, p. 2114, 2018.

[4] B. Alberts *et al.*, *Molecular Biology of the Cell*, 6th ed. 2015.

[5] J. D. Watson and F. H. C. Crick, “A Structure for Deoxyribose Nucleic Acid,” *Nature*, vol. 171, no. 4356, pp. 737–738, 1953.

[6] M. H. F. Wilkins, A. R. Stokes, and H. R. Wilson, “Molecular Structure of Deoxypentose Nucleic Acids,” *Nature*, vol. 171, pp. 738–740, 1953.

[7] R. E. Franklin and R. G. Gosling, “Molecular Configuration in Sodium Thymonucleate,” *Nature*, vol. 171, pp. 740–741, 1953.

[8] D. L. Nelson and M. M. Cox, *Lehninger Principles of Biochemistry*, 4th ed. W. H. Freeman, 2005.

[9] J. M. Berg, J. L. Tymoczko, L. Stryer, and G. J. Gatto, *Biochemistry*, 7th ed. 2012.

[10] E. T. Kool, “Hydrogen bonding, base stacking, and steric effects in DNA replication,” *Annu. Rev. Biophys. Biomol. Struct.*, vol. 30, pp. 1–22, 2001.

[11] F. Kilchherr, C. Wachauf, B. Pelz, M. Rief, M. Zacharias, and H. Dietz, “Single-molecule dissection of stacking forces in DNA,” *Science (80-.).*, vol. 353, no. 6304, p. 1116, 2016.

[12] G. M. Blackburn, M. J. Gait, D. Loakes, and D. M. Williams, *Nucleic Acids in Chemistry and Biology*, 3rd ed. RSC Publishing, 2006.

[13] S. Benabou, A. Aviñó, R. Eritja, C. González, and R. Gargallo, “Fundamental aspects of the nucleic acid i-motif structures,” *RSC Adv.*, vol. 4, no. 51, pp. 26956–26980, 2014.

[14] A. R. Chandrasekaran and D. A. Rusling, “Triplex-forming oligonucleotides: A third strand for DNA nanotechnology,” *Nucleic Acids Res.*, vol. 46, no. 3, pp. 1021–1037, 2018.

[15] P. L. James, T. Brown, and K. R. Fox, “Thermodynamic and kinetic stability of intermolecular triple helices containing different proportions of C+GC and TAT triplets,” *Nucleic Acids Res.*, vol. 31, no. 19, pp. 5598–5606, 2003.

[16] Y. Hu, A. Cecconello, A. Idili, F. Ricci, and I. Willner, “Triplex DNA

Nanostructures: From Basic Properties to Applications," *Angew. Chemie - Int. Ed.*, vol. 56, no. 48, pp. 15210–15233, 2017.

[17] N. C. Seeman, "Nucleic acid junctions and lattices," *J. Theor. Biol.*, 1982.

[18] S. Nummelin, J. Kommeri, M. A. Kostiainen, and V. Linko, "Evolution of Structural DNA Nanotechnology," *Adv. Mater.*, vol. 30, no. 24, p. 1703721, 2018.

[19] F. C. Simmel, "DNA origami - art, science, and engineering," *Front. Life Sci.*, vol. 6, no. 1–2, pp. 3–9, 2012.

[20] N. C. Seeman, "Nanomaterials Based on DNA," *Annu. Rev. Biochem.*, vol. 79, no. 1, pp. 65–87, 2010.

[21] S. N. Cohen, A. C. Y. Chang, H. W. Boyer, and R. B. Helling, "Construction of Biologically Functional Bacterial Plasmids In Vitro," *Proc. Natl. Acad. Sci.*, vol. 70, no. 11, pp. 3240–3244, 1973.

[22] H. Qiu, J. C. Dewan, and N. C. Seeman, "A DNA Decamer with a Sticky End: The Crystal Structure of d-CGACGATCGT," *J. Mol. Biol.*, vol. 267, pp. 881–898, 1997.

[23] R. Holliday, "A mechanism for gene conversion in fungi," *Genet. Res. (Camb).*, vol. 89, no. 5, pp. 282–304, 1964.

[24] N. C. Seeman, "Biochemistry and Structural DNA Nanotechnology: An Evolving Symbiotic Relationship," *Biochemistry*, vol. 42, no. 24, pp. 7259–7269, 2003.

[25] F. Praetorius, B. Kick, K. L. Behler, M. N. Honemann, D. Weuster-Botz, and H. Dietz, "Biotechnological mass production of DNA origami," *Nature*, vol. 552, no. 7683, pp. 84–87, 2017.

[26] N. R. Kallenbach, R.-I. Ma, and N. C. Seeman, "An immobile nucleic acid junction constructed from oligonucleotides," *Nature*, vol. 305, no. 27, pp. 829–831, 1983.

[27] E. Winfree, F. Liu, L. A. Wenzler, and N. C. Seeman, "Design and self-assembly of two-dimensional DNA crystals," *Nature*, vol. 394, no. 6693, pp. 539–544, 1998.

[28] F. Tsu-Ju and N. C. Seeman, "DNA Double-Crossover Molecules," *Biochemistry*, vol. 32, no. 13, pp. 3211–3220, 1993.

[29] D. Yang, M. J. Campolongo, T. N. Nhi Tran, R. C. H. Ruiz, J. S. Kahn, and D. Luo, "Novel DNA materials and their applications," *Wiley Interdiscip. Rev. Nanomedicine Nanobiotechnology*, vol. 2, no. 6, pp. 648–669, 2010.

[30] T. H. LaBean *et al.*, "Construction, analysis, ligation, and self-assembly of DNA triple crossover complexes," *J. Am. Chem. Soc.*, vol. 122, no. 9, pp. 1848–1860, 2000.

[31] Z. Shen, H. Yan, T. Wang, and N. C. Seeman, “Paranemic Crossover DNA: A Generalized Holliday Structure with Applications in Nanotechnology,” *J. Am. Chem. Soc.*, vol. 126, no. 6, pp. 1666–1674, 2004.

[32] H. Yan, X. Zhang, Z. Shen, and N. C. Seeman, “A robust DNA mechanical device controlled by hybridization topology,” *Nature*, vol. 415, no. 6867, pp. 62–65, 2002.

[33] V. Linko and H. Dietz, “The enabled state of DNA nanotechnology,” *Curr. Opin. Biotechnol.*, vol. 24, no. 4, pp. 555–561, 2013.

[34] M. Bathe and P. W. K. Rothemund, “DNA Nanotechnology: A foundation for Programmable Nanoscale Materials,” *MRS Bull.*, vol. 42, no. 12, pp. 882–888, 2017.

[35] F. Hong, F. Zhang, Y. Liu, and H. Yan, *DNA Origami: Scaffolds for Creating Higher Order Structures*, vol. 117, no. 20. 2017.

[36] P. Wang, T. A. Meyer, V. Pan, P. K. Dutta, and Y. Ke, “The Beauty and Utility of DNA Origami,” *Chem*, vol. 2, no. 3, pp. 359–382, 2017.

[37] V. Linko, A. Ora, and M. A. Kostiainen, “DNA Nanostructures as Smart Drug-Delivery Vehicles and Molecular Devices,” *Trends Biotechnol.*, vol. 33, no. 10, pp. 586–594, 2015.

[38] J. Li, C. Fan, H. Pei, J. Shi, and Q. Huang, “Smart drug delivery nanocarriers with self-assembled DNA nanostructures,” *Adv. Mater.*, vol. 25, no. 32, pp. 4386–4396, 2013.

[39] B. R. Madhanagopal, S. Zhang, E. Demirel, H. Wady, and A. R. Chandrasekaran, “DNA Nanocarriers: Programmed to Deliver,” *Trends Biochem. Sci.*, vol. 43, no. 12, pp. 997–1013, 2018.

[40] Y. Zhang *et al.*, “Programmable and Multifunctional DNA-Based Materials for Biomedical Applications,” *Adv. Mater.*, vol. 30, no. 24, p. 1703658, 2018.

[41] V. Linko, S. Nummelin, L. Aarnos, K. Tapio, J. Toppari, and M. Kostiainen, “DNA-Based Enzyme Reactors and Systems,” *Nanomaterials*, vol. 6, no. 8, p. 139, 2016.

[42] J. Pan, F. Li, T. G. Cha, H. Chen, and J. H. Choi, “Recent progress on DNA based walkers,” *Curr. Opin. Biotechnol.*, vol. 34, pp. 56–64, 2015.

[43] J. Bath and A. J. Turberfield, “DNA nanomachines,” *Nat. Nanotechnol.*, vol. 2, pp. 275–284, 2007.

[44] A. Kuzyk, R. Jungmann, G. P. Acuna, and N. Liu, “DNA Origami Route for Nanophotonics,” *ACS Photonics*, vol. 5, no. 4, pp. 1151–1163, 2018.

[45] N. Liu and T. Liedl, “DNA-Assembled Advanced Plasmonic Architectures,” *Chem. Rev.*, vol. 118, no. 6, pp. 3032–3053, 2018.

[46] B. Shen, M. A. Kostiainen, and V. Linko, “DNA Origami Nanophotonics and

Plasmonics at Interfaces," *Langmuir*, vol. 34, no. 49, pp. 14911–14920, 2018.

[47] G. Grossi, M. D. E. Jepsen, J. Kjems, and E. S. Andersen, "Control of enzyme reactions by a reconfigurable DNA nanovault," *Nat. Commun.*, vol. 8, no. 1, p. 992, 2017.

[48] V. Linko, M. Eerikäinen, and M. A. Kostiainen, "A modular DNA origami-based enzyme cascade nanoreactor," *Chem. Commun.*, vol. 51, no. 25, pp. 5351–5354, 2015.

[49] J. S. Shin and N. A. Pierce, "A synthetic DNA walker for molecular transport," *J. Am. Chem. Soc.*, vol. 126, no. 35, pp. 10834–10835, 2004.

[50] A. Kuzyk *et al.*, "DNA-based self-assembly of chiral plasmonic nanostructures with tailored optical response," *Nature*, vol. 483, no. 7389, pp. 311–314, 2012.

[51] A. Kuzuya and M. Komiyama, "DNA origami: Fold, stick, and beyond," *Nanoscale*, vol. 2. pp. 310–322, 2010.

[52] D. Han, S. Pal, Y. Liu, and H. Yan, "Folding and cutting DNA into reconfigurable topological nanostructures," *Nat. Nanotechnol.*, vol. 5, no. 10, pp. 712–717, 2010.

[53] D. Han, S. Pal, J. Nangreave, Z. Deng, Y. Liu, and H. Yan, "DNA Origami with Complex Curvatures in Three-Dimensional Space," *Science (80-.).*, vol. 332, pp. 342–346, 2011.

[54] E. S. Andersen *et al.*, "Self-assembly of a nanoscale DNA box with a controllable lid," *Nature*, vol. 459, no. 7243, pp. 73–76, 2009.

[55] Y. Ke *et al.*, "Multilayer DNA origami packed on a square lattice," *J. Am. Chem. Soc.*, vol. 131, no. 43, pp. 15903–15908, 2009.

[56] S. M. Douglas, H. Dietz, T. Liedl, B. Högberg, F. Graf, and W. M. Shih, "Self-assembly of DNA into nanoscale three-dimensional shapes," *Nature*, vol. 459, no. 7245, pp. 414–418, 2009.

[57] Y. Ke, N. V. Voigt, K. V. Gothelf, and W. M. Shih, "Multilayer DNA origami packed on hexagonal and hybrid lattices," *J. Am. Chem. Soc.*, vol. 134, no. 3, pp. 1770–1774, 2012.

[58] H. Dietz, S. M. Douglas, and W. M. Shih, "Folding DNA into Twisted and Curved Nanoscale Shapes," *Science (80-.).*, vol. 325, no. 5941, pp. 725–730, 2009.

[59] C. E. Castro *et al.*, "A primer to scaffolded DNA origami," *Nat. Methods*, vol. 8, no. 3, pp. 221–229, 2011.

[60] S. M. Douglas, A. H. Marblestone, S. Teerapittayanon, A. Vazquez, G. M. Church, and W. M. Shih, "Rapid prototyping of 3D DNA-origami shapes with caDNAno," *Nucleic Acids Res.*, vol. 37, no. 15, pp. 5001–5006, 2009.

[61] D. N. Kim, F. Kilchherr, H. Dietz, and M. Bathe, "Quantitative prediction of 3D solution shape and flexibility of nucleic acid nanostructures," *Nucleic Acids*

Res., vol. 40, no. 7, pp. 2862–2868, 2012.

[62] C. Maffeo, J. Yoo, and A. Aksimentiev, “De novo reconstruction of DNA origami structures through atomistic molecular dynamics simulation,” *Nucleic Acids Res.*, vol. 44, no. 7, pp. 3013–3019, 2016.

[63] E. Benson *et al.*, “DNA rendering of polyhedral meshes at the nanoscale,” *Nature*, vol. 523, no. 7561, pp. 441–444, 2015.

[64] R. Veneziano *et al.*, “Designer nanoscale DNA assemblies programmed from the top down,” *Science (80-.).*, vol. 352, no. 6293, p. 1534, 2016.

[65] Yin, Y. Ke, L. L. Ong, and W. M. Shih, “Three-dimensional structures self-assembled from DNA bricks.,” *Sci. (New York)*, vol. 338, no. November, pp. 1177–1184, 2012.

[66] T. Gerling, K. F. Wagenbauer, A. M. Neuner, and H. Dietz, “Dynamic DNA devices and assemblies formed by shape-complementary, non-base pairing 3D components,” *Science (80-.).*, vol. 347, no. 6229, pp. 1446–1452, 2015.

[67] K. F. Wagenbauer *et al.*, “How We Make DNA Origami,” *ChemBioChem*, vol. 18, no. 19, pp. 1873–1885, 2017.

[68] B. Saccà and C. M. Niemeyer, “DNA origami: The art of folding DNA,” *Angew. Chemie - Int. Ed.*, vol. 51, no. 1, pp. 58–66, 2012.

[69] E. Pound, J. R. Ashton, H. A. Becerril, and A. T. Woolley, “Polymerase chain reaction based scaffold preparation for the production of thin, branched DNA origami nanostructures of arbitrary sizes,” *Nano Lett.*, vol. 9, no. 12, pp. 4302–4305, 2009.

[70] H. Zhang, J. Chao, D. Pan, H. Liu, Q. Huang, and C. Fan, “Folding super-sized DNA origami with scaffold strands from long-range PCR,” *Chem. Commun.*, vol. 48, pp. 6405–6407, 2012.

[71] T. R. Shepherd, R. R. Du, H. Huang, E. Wamhoff, and M. Bathe, “Bioproduction of single-stranded DNA from isogenic miniphage,” bioRxvi doi: 10.1101/521443, 2019.

[72] H. Said, V. J. Schüller, F. J. Eber, C. Wege, T. Liedl, and C. Richert, “M1.3 - A small scaffold for DNA origami,” *Nanoscale*, vol. 5, no. 1, pp. 284–290, 2013.

[73] B. Högberg, T. Liedl, and W. M. Shih, “Folding DNA Origami from a Double-Stranded Source of Scaffold,” *J. Am. Chem. Soc.*, vol. 131, no. 26, pp. 9154–9155, 2009.

[74] T. G. Martin and H. Dietz, “Magnesium-free self-assembly of multi-layer DNA objects,” *Nat. Commun.*, vol. 3, p. 1103, 2012.

[75] C. Kielar *et al.*, “On the Stability of DNA Origami Nanostructures in Low-Magnesium Buffers,” *Angew. Chemie - Int. Ed.*, vol. 57, no. 30, pp. 9470–9474, 2018.

[76] E. Stahl, T. G. Martin, F. Praetorius, and H. Dietz, “Facile and scalable preparation of pure and dense DNA origami solutions,” *Angew. Chemie - Int. Ed.*, vol. 53, no. 47, pp. 12735–12740, 2014.

[77] C. Lin, S. D. Perrault, M. Kwak, F. Graf, and W. M. Shih, “Purification of DNA-origami nanostructures by rate-zonal centrifugation,” *Nucleic Acids Res.*, vol. 41, no. 2, p. e40, 2013.

[78] S. M. Douglas, I. Bachelet, G. M. Church, E. Winfree, and T. H. LaBean, “A Logic-Gated Nanorobot for Targeted Transport of Molecular Payloads,” *Science (80-.).*, vol. 335, no. 6070, pp. 831–834, 2012.

[79] A. Shaw, E. Benson, and B. Högberg, “Purification of functionalized DNA origami nanostructures,” *ACS Nano*, vol. 9, no. 5, pp. 4968–4975, 2015.

[80] M. Adrian, J. Dubochet, J. Lepault, and A. W. McDowall, “Cryo-electron microscopy of viruses,” *Nature*, vol. 308, no. 5954, pp. 32–36, 1984.

[81] N. C. Seeman, C. Mao, W. Sun, and Z. Shen, “A nanomechanical device based on the B-Z transition of DNA,” *Nature*, vol. 397, no. 6715, pp. 144–146, 1999.

[82] B. Yurke, A. J. Turberfield, A. P. Mills, F. C. Simmel, and J. L. Neumann, “A DNA-fuelled molecular machine made of DNA,” *Nature*, vol. 406, no. 6796, pp. 605–608, 2000.

[83] A. Idili, A. Vallée-Bélisle, and F. Ricci, “Programmable pH-triggered DNA nanoswitches,” *J. Am. Chem. Soc.*, vol. 136, no. 16, pp. 5836–5839, 2014.

[84] A. Kuzyk, M. J. Urban, A. Idili, F. Ricci, and N. Liu, “Selective control of reconfigurable chiral plasmonic metamolecules,” *Sci. Adv.*, vol. 3, no. 4, p. e1602803, 2017.

[85] Y. Hu, J. Ren, C. H. Lu, and I. Willner, “Programmed pH-driven reversible association and dissociation of interconnected circular DNA dimer nanostructures,” *Nano Lett.*, vol. 16, no. 7, pp. 4590–4594, 2016.

[86] N. Wu and I. Willner, “pH-Stimulated Reconfiguration and Structural Isomerization of Origami Dimer and Trimer Systems,” *Nano Lett.*, vol. 16, no. 10, pp. 6650–6655, 2016.

[87] A. Ottaviani, F. Iacovelli, A. Idili, M. Falconi, F. Ricci, and A. Desideri, “Engineering a responsive DNA triple helix into an octahedral DNA nanostructure for a reversible opening/closing switching mechanism: a computational and experimental integrated study,” *Nucleic Acids Res.*, vol. 46, no. 19, pp. 9951–9959, 2018.

[88] S. H. Kim, K. R. Kim, D. R. Ahn, J. E. Lee, E. G. Yang, and S. Y. Kim, “Reversible Regulation of Enzyme Activity by pH-Responsive Encapsulation in DNA Nanocages,” *ACS Nano*, vol. 11, no. 9, pp. 9352–9359, 2017.

[89] J. R. Burns, B. Lamarre, A. L. B. Pyne, J. E. Noble, and M. G. Ryadnov, “DNA Origami Inside-Out Viruses,” *ACS Synth. Biol.*, vol. 7, no. 3, pp. 767–773, 2018.

[90] T. Takenaka *et al.*, “Photoresponsive DNA nanocapsule having an open/close system for capture and release of nanomaterials,” *Chem. - A Eur. J.*, vol. 20, no. 46, pp. 14951–14954, 2014.

[91] J. R. Lakowicz, “Energy Transfer,” in *Principles of Fluorescence Spectroscopy*, Third edit., 2006, pp. 443–476.

[92] A. J. P. Teunissen, C. Pérez-Medina, A. Meijerink, and W. J. M. Mulder, “Investigating supramolecular systems using Förster resonance energy transfer,” *Chem. Soc. Rev.*, vol. 47, no. 18, pp. 7027–7044, 2018.

[93] H. Sahoo, “Förster resonance energy transfer - A spectroscopic nanoruler: Principle and applications,” *J. Photochem. Photobiol. C Photochem. Rev.*, vol. 12, no. 1, pp. 20–30, 2011.

[94] L. Ma, F. Yang, and J. Zheng, “Application of fluorescence resonance energy transfer in protein studies,” *J. Mol. Struct.*, vol. 1077, pp. 87–100, 2014.

[95] S. Farooq, C. Fijen, and J. Hohlbein, “Studying DNA-protein interactions with single-molecule Förster resonance energy transfer,” *Protoplasma*, vol. 251, no. 2, pp. 317–332, 2014.

[96] R. Roy, S. Hohng, and T. Ha, “A practical guide to single-molecule FRET,” *Nat. Methods*, vol. 5, no. 6, pp. 507–516, 2008.

[97] J. Chen, N. K. Poddar, L. J. Tauzin, D. Cooper, A. B. Kolomeisky, and C. F. Landes, “Single-molecule FRET studies of HIV TAR-DNA hairpin unfolding dynamics,” *J. Phys. Chem. B*, vol. 118, no. 42, pp. 12130–12139, 2014.

[98] S. L. Noer, S. Preus, D. Gudnason, M. Aznauryan, J. L. Mergny, and V. Birkedal, “Folding dynamics and conformational heterogeneity of human telomeric G-quadruplex structures in Na+solutions by single molecule FRET microscopy,” *Nucleic Acids Res.*, vol. 44, no. 1, pp. 464–471, 2016.

[99] R. M. Clegg, A. I. H. Murchie, A. Zechel, C. Carlberg, S. Diekmann, and D. M. Lilley, “Fluorescence Resonance Energy Transfer Analysis of the Structure of the Four-Way DNA Junction,” *Biochemistry*, vol. 31, no. 20, pp. 4846–4856, 1992.

[100] R. M. Zadegan *et al.*, “Construction of a 4 Zeptoliters switchable 3D DNA box origami,” *ACS Nano*, vol. 6, no. 11, pp. 10050–10053, 2012.

[101] A. S. Walsh, H. Yin, C. M. Erben, M. J. A. Wood, and A. J. Turberfield, “DNA cage delivery to mammalian cells,” *ACS Nano*, vol. 5, no. 7, pp. 5427–5432, 2011.

[102] R. Tsukanov, T. E. Tomov, M. Liber, Y. Berger, and E. Nir, “Developing DNA nanotechnology using single-molecule fluorescence,” *Acc. Chem. Res.*, vol. 47, no. 6, pp. 1789–1798, 2014.

[103] D. Selnihhin, S. M. Sparvath, S. Preus, V. Birkedal, and E. S. Andersen, “Multifluorophore DNA Origami Beacon as a Biosensing Platform,” *ACS Nano*, vol. 12, no. 6, pp. 5699–5708, 2018.

[104] Y. Choi, L. Kotthoff, L. Olejko, U. Resch-Genger, and I. Bald, “DNA Origami-Based Förster Resonance Energy-Transfer Nanoarrays and Their Application as Ratiometric Sensors,” *ACS Appl. Mater. Interfaces*, vol. 10, no. 27, pp. 23295–23302, 2018.

[105] S. Modi, M. G. Swetha, D. Goswami, G. D. Gupta, S. Mayor, and Y. Krishnan, “A DNA nanomachine that maps spatial and temporal pH changes inside living cells,” *Nat. Nanotechnol.*, vol. 4, no. 5, pp. 325–330, 2009.

[106] N. Xie *et al.*, “Scallop-Inspired DNA Nanomachine: A Ratiometric Nanothermometer for Intracellular Temperature Sensing,” *Anal. Chem.*, vol. 89, no. 22, pp. 12115–12122, 2017.

[107] J. J. Schmied *et al.*, “DNA origami – based standards for quantitative fluorescence microscopy,” *Nat. Protoc.*, vol. 9, no. 6, pp. 1367–1391, 2014.

[108] J. J. Schmied *et al.*, “DNA Origami Nanopillars as Standards for Three-Dimensional Superresolution Microscopy,” *Nano Lett.*, vol. 13, pp. 781–785, 2013.

[109] I. H. Stein, V. Schüller, P. Böhm, P. Tinnefeld, and T. Liedl, “Single-Molecule FRET Ruler Based on Rigid DNA Origami Blocks,” *ChemPhysChem*, vol. 12, pp. 689–695, 2011.

[110] M. Raab, J. J. Schmied, I. Jusuk, C. Forthmann, P. Tinnefeld, and M. Carlo, “Fluorescence Microscopy with 6 nm Resolution on DNA Origami,” *ChemPhysChem*, vol. 15, pp. 2431–2435, 2014.

[111] E. Graugnard, W. L. Hughes, R. Jungmann, M. A. Kostiainen, and V. Linko, “Nanometrology and super-resolution imaging with DNA,” *MRS Bull.*, vol. 42, no. 12, pp. 951–959, Dec. 2017.

[112] X. Wei, J. Nangreave, S. Jiang, H. Yan, and Y. Liu, “Mapping the thermal behavior of DNA origami nanostructures,” *J. Am. Chem. Soc.*, vol. 135, no. 16, pp. 6165–6176, 2013.

[113] B. Valeur, *Molecular Fluorescence: Principles and Applications*, 1st ed. Wiley-VCH Verlag GmbH, 2001.

[114] H. C. Cheung, *Topics in Fluorescence Spectroscopy*. Kluwer Academic Publishers, 2002.

[115] S. Preus and L. M. Wilhelmsson, “Advances in Quantitative FRET-Based Methods for Studying Nucleic Acids,” *ChemBioChem*, vol. 13, pp. 1990–2001, 2012.

[116] H. Ijäs, I. Hakaste, B. Shen, M. A. Kostiainen, and V. Linko, “Reconfigurable and Programmable pH-Responsive DNA Origami Nanocapsule for Loading, Encapsulation and Displaying of Cargo,” submitted for publibcation, 2019.

[117] “Integrated DNA Technologies Inc.” [Online]. Available: https://eu.idtdna.com/site/Catalog/Modifications/Dyes. [Accessed: 24-Jan-2019].

[118] B. A. Webb, M. Chimenti, M. P. Jacobson, and D. L. Barber, “Dysregulated pH: A perfect storm for cancer progression,” *Nat. Rev. Cancer*, vol. 11, no. 9, pp. 671–677, 2011.

[119] H. Auvinen *et al.*, “Protein Coating of DNA Nanostructures for Enhanced Stability and Immunocompatibility,” *Adv. Healthcare Mater.*, vol. 6, no. 18, 2017.

[120] S. Ramakrishnan, H. Ijäs, V. Linko, and A. Keller, “Structural stability of DNA origami nanostructures under application-specific conditions,” *Comput. Struct. Biotechnol. J.*, vol. 16, pp. 342–349, 2018.

Appendix A: Additional TEM images

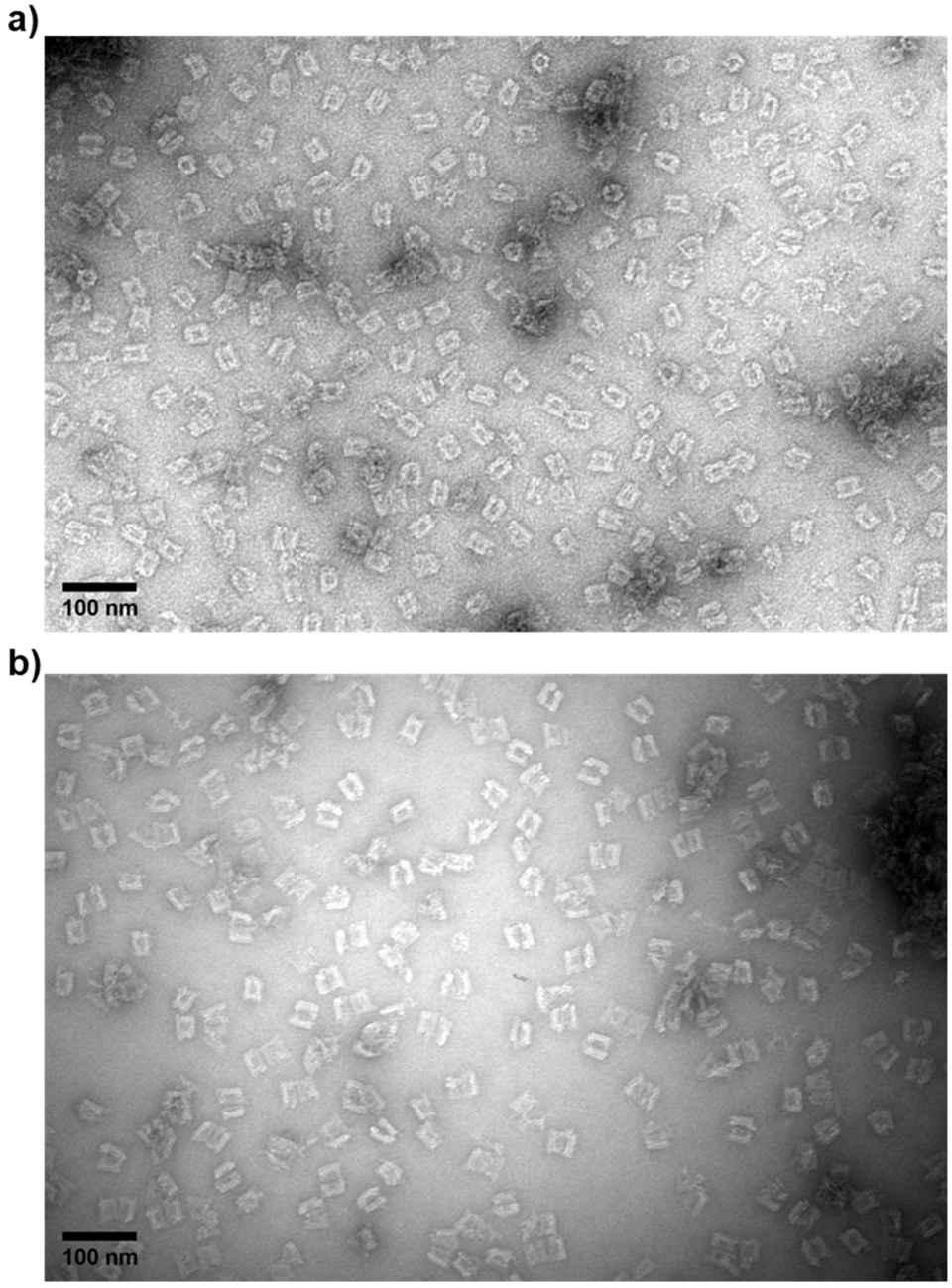

Figure A1: TEM images of closed and open controls. a) Closed control sample. b) Open control sample. Adapted from [116].

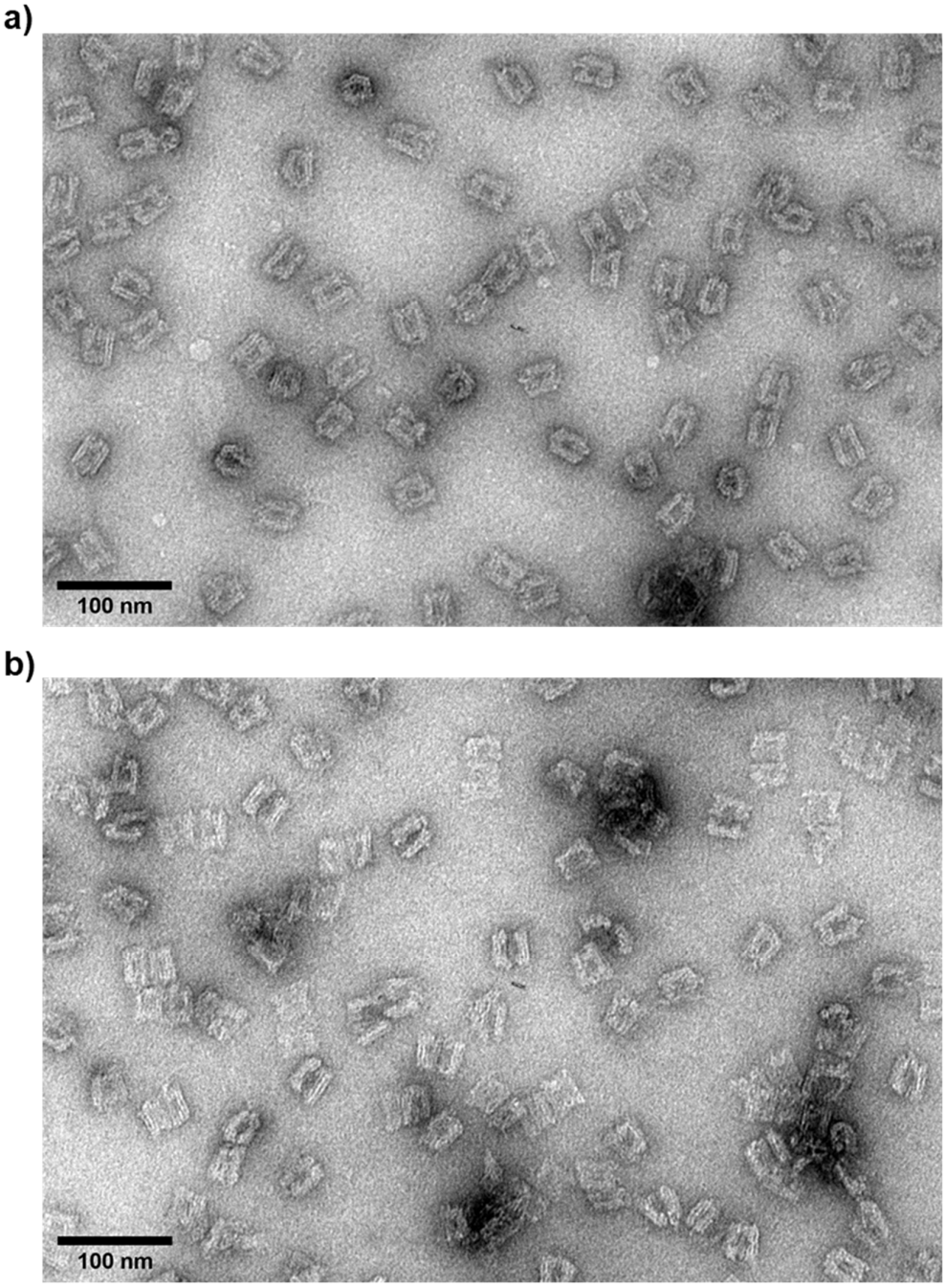

Figure A2: TEM images of pH-latch capsule at different pHs. a) pH-latch sample at pH 6.2. b) pH-latch sample at pH 8.2. Adapted from [116].

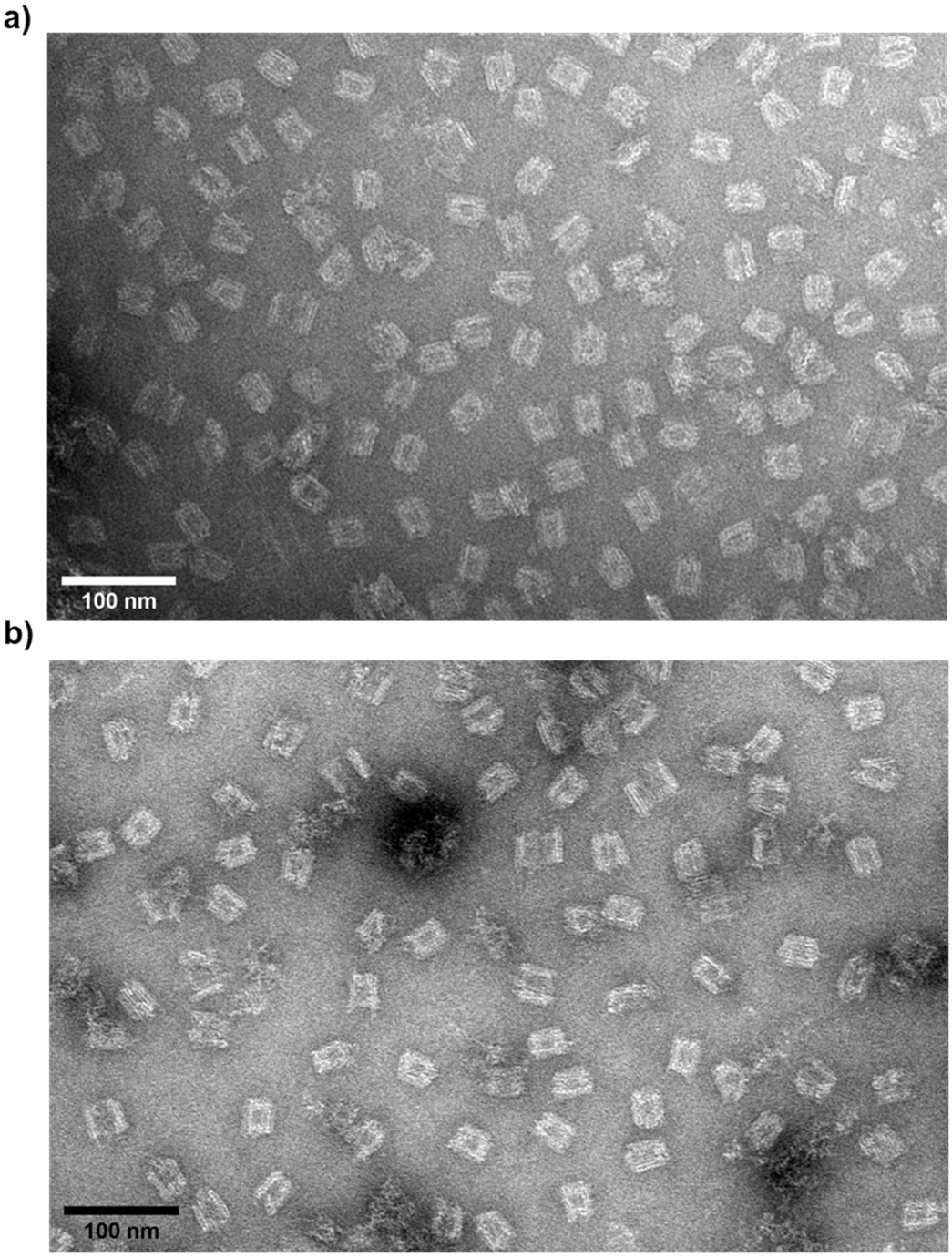

Figure A3: TEM images of closed capsule samples from the five-cycle experiment. a) Closed control sample after first acetic acid addition. b) Closed control sample after fifth acetic acid addition. Adapted from [116].